# Engineered inorganic core/shell nanoparticles

Patrice Mélinon

*Institut Lumière matière Université Claude Bernard Lyon 1 et CNRS et OMNT Domaine Scientifique de la Doua, Bâtiment Léon Brillouin 43 Boulevard du 11 Novembre 1918 F 69622 Villeurbanne, France*

Sylvie Begin-Colin

*IPCMS et OMNT 23 rue du Loess BP 43 67034 STRASBOURG Cedex 2 France*

Jean Luc Duvail

*IMN -UMR6502 et OMNT Campus Sciences : 2 rue de la Houssinire, BP32229, 44322 Nantes cedx3, France*

Fabienne Gauffre

*SPM et OMNT : Institut des sciences chimiques de Rennes - UMR 6226 263 Avenue du General Leclerc CS 74205 35042 RENNES Cedex, France*

Nathalie Herlin Boime

*, IRAMIS-NIMBE, Laboratoire Francis Perrin (CEA CNRS URA 2453) et OMNT, Bat 522, CEA Saclay, 91919 Gif/Yvette Cedex France*

Gilles Ledoux

*Institut Lumière matière Université Claude Bernard Lyon 1 et CNRS et OMNT Domaine Scientifique de la Doua, Bâtiment Alfred Kastler 43 Boulevard du 11 Novembre 1918 F 69622 Villeurbanne, France*

Jérôme Plain

*Universit de technologie de Troyes LNIO-ICD , CNRS et OMNT 12 rue Marie Curie - CS 42060 - 10004 Troyes cedex, France*

Peter Reiss

*CEA Grenoble, INAC-SPrAM,UMR 5819 CEA-CNRS-UJF et OMNT, Grenoble cedex 9, France*

Fabien Silly

*CEA, IRAMIS, SPEC, TITANS, CNRS 2464 et OMNT, F-91191 Gif sur Yvette, France*

*Preprint submitted to Physics Reports* *June 6, 2014*

Bénédicte Warot-Fonrose

*CEMES-CNRS, Université de Toulouse et OMNT 29 rue Jeanne Marvig F 31055 Toulouse, France*

**Abstract**

It has been for a long time recognized that nanoparticles are of great scientific interest as they are effectively a bridge between bulk materials and atomic structures. At first, size effects occurring in single elements have been studied. More recently, progress in chemical and physical synthesis routes permitted the preparation of more complex structures. Such structures take advantages of new adjustable parameters including stoichiometry, chemical ordering, shape and segregation opening new fields with tailored materials for biology, mechanics, optics magnetism, chemistry catalysis, solar cells and microelectronics. Among them, core/shell structures are a particular class of nanoparticles made with an inorganic core and one or several inorganic shell layer(s). In earlier work, the shell was merely used as a protective coating for the core. More recently, it has been shown that it is possible to tune the physical properties in a larger range than that of each material taken separately. The goal of the present review is to discuss the basic properties of the different types of core/shell nanoparticles including a large variety of heterostructures. We restrict ourselves on all inorganic (on inorganic/inorganic) core/shell structures. In the light of recent developments, the applications of inorganic core/shell particles are found in many fields including biology, chemistry, physics and engineering. In addition to a representative overview

of the properties, general concepts based on solid state physics are considered for material selection and for identifying criteria linking the core/shell structure and its resulting properties. Chemical and physical routes for the synthesis and specific methods for the study of core/shell nanoparticle are briefly discussed.

*Keywords:* nanoparticle, core shell, synthesis, plasmonics

## 1. Introduction

Nanoparticles Nps can be considered as a new state of matter building a bridge between bulk materials and atomic or molecular structures. A bulk material should have constant physical properties regardless of its size, however at the nano-scale size-dependent properties are often observed. It is generally admitted that size effects occur when the physical characteristic length under consideration is of the same order of magnitude as the size. Furthermore, at the nanoscale quantum effects illustrated by rehybridization or charge transfer affect the properties of the elements leading to "novel properties". At first, size effects occurring in single elements have been studied. More recently, progress in chemical and physical synthesis routes permitted the preparation of binary and more complex structures. Such structures take advantages of new adjustable parameters including stoichiometry, chemical ordering, shape and segregation. In this regard, such complex nanostructures have also become of interest as they offer additional degrees of freedom opening new fields with tailored materials for biology [1], mechanics [2], optics [3, 4], magnetism [5], chemistry [6] catalysis (including photocatalysis [7]), solar cells [8] and microelectronics. Among them, core/shell structures

[9] are a particular class of NPs consisting of an inorganic core and one or several inorganic shell layer(s). In earlier works, the shell was merely used as a protective coating for the core. In this case the shell acts as a barrier against impinging atoms or ions making the nanocrystals less sensitive to environmental changes [10]. Moreover the shell contributes to the passivation of the core surface suppressing surface electronic trap states. The former feature is well evidenced in electrochemistry where electrodes remain effective for a long time in fuel cells and batteries [11]. The latter is illustrated by the enhanced fluorescence quantum yield of semiconducting nanocrystals upon overgrowth with an appropriate shell. In the field of catalysis, core/shell structures enable atom economy of precious catalyst metals by using them only in the shell while applying an inert core material as support. Core/shell structures are also used in solid state reaction metallurgy where the particle growth can be done in a 'size focusing' regime allowing strategies for manipulating precipitates narrow size distributions [12]. More recently, by the appropriate choice of the core and shell materials, it has been shown that it is possible to tune the properties (optical, reactivity ,magnetic /ldots) in a spectral window larger than the window of each material taken separately [13]. This review mainly focuses on systems with specific properties arising from the core/shell structure. These properties are due to the polarization, rehybridization or charge transfer induced by the difference between both constituents. The interface between the two elements is of prime importance. The goal of the present review is to discuss the basic properties of the different types of core/shell NPs including a large variety of heterostructures: metal/metal, metal/semiconductor (or insulator), semiconductor/ semicon-

ductor [14] and insulator/insulator. We restrict ourselves mainly on inorganic core/shell structures, possibly stabilized by organic ligands in the colloidal state. Core/shell structures have found applications in many fields including biology, chemistry, physics and engineering. Among numerous review papers [14, 9, 3] dedicated to core/shell structures, we focus on a representative overview of their physical aspects. In addition, we discuss general considerations for the choice of materials starting from a solid state physics point of view, considering the core/shell structure as ultimate segregated system where the shell perfectly wets the core. The resulting criteria for core/shell structure predictions and related properties, especially the coupling between NPs and surrounding medium through plasmonic properties, are aimed to be of practical use for the interested reader. Chemical and physical routes for the synthesis and specific methods for the study of core/shell NPs are also briefly discussed.

## 2. Synthesis of core/shell structures

### *2.1. Chemical route*

There is a large panel of chemical synthesis methods for colloidal inorganic NPs. The chemical synthesis of core/shell NPs can be roughly divided into two main strategies: 1) Synthesis of the core NPs, followed by the shell growth on their surface. This method is by far the most widely applied procedure. 2) cation exchange

#### *2.1.1. Synthesis of the core nanoparticles*

In the case of oxide core/shell NPs, the main methods to synthesize the core comprise 1) synthesis in aqueous systems (co-precipitation, sol-gel ...)

by precipitation of reagents and 2) solvothermal methods based on the decomposition of metal precursors in presence of surfactants. This decomposition may be induced by different energy sources (thermal, microwave, light ...). Then the core is coated either by an inorganic ceramic or metallic coating and silica are among the most reported and used coating. For the generation of silica coatings on the surface of metal oxide and magnetic NPs, the Stöber method and sol-gel [11] processes are the most common choices. The Stöber method relies on the addition of tetraethoxysilane (TEOS) to NPs dispersed in aqueous phase in presence of an alcohol (e.g. ethanol) and ammonium hydroxide. The thickness of the coating can generally be tuned by varying the concentration of ammonium hydroxide and the ratio of TEOS to $H_2O$. In microemulsion synthesis [15, 16] micelles (e.g. Stöber process) or inverse micelles are used to confine and control the silica coating on core NPs. While a controlled silica shell thickness can be obtained, a drawback of this method is the difficult separation of the core/shell NPs from the large amount of surfactants associated with the microemulsion system. Aerosol pyrolysis has also been used for silica coating, but the structure of the composite NPs is commonly of "mosaic type", such as hollow silica spheres with iron oxide shells [17, 18]. To overcome shortcomings related to many aqueous synthesis processes, which concern colloidal stability, (i.e. NPs aggregation state) and final particle size, the synthesis of core/shell particles in organic solvents using solvothermal methods is widely developed. It affords further improved control over size and shape and thus higher modulation in core/shell structures and in the resulting properties [19, 20]. Solvothermal methods lead to ligand coated NPs and thus to stable suspensions of isolated (non aggregated)

particles in organic solvents.

In the case of semiconductor/semiconductor or (oxyde or metal) magnetic/magnetic core/shell nanocrystals, shell growth is mainly carried out in the same high boiling point organic solvents as for the core synthesis following a seed-mediated growth approach [14, 21, 22]. After the core synthesis, the shell precursors are generally slowly added or fully added with a controlled amount in order to avoid homogeneous nucleation of the shell material. Using such a seed mediated growth approach several type of oxide/oxide ($M_xFe_{3-x}O4/Fe_xM'_{3-x}O_4$ with M or M'=Fe, Zn, Ni, Mn) or metal/oxide (often $Fe_3 - XO_4$/Au)or metal/metal (M/M' with M or M' = Au, Ag, Fe, Co, FePt, CoPt ...)and the inverted structures have been synthesized. The thickness of the shell is mainly controlled by the introduced amount of shell precursor but the size of core may influence the growth of the shell leading either to core-shell or dumbell or flower structures [23, 24, 25].

A variant, leading to a very good control of the shell thickness, is the so-called SILAR (selective ion layer adsorption and reaction) method. Here, a precisely calculated amount of the cation and anion precursors are added in an alternating manner, so that at each step half of a monolayer is formed. The most well known system in this context is CdSe/CdS [26, 27], for which a very narrow size distribution could be obtained even for very thick shells ($>$ 10 monolayers). In the case of semiconductor nanocrystals obtained by aqueous synthesis, shell growth is mainly performed by the decomposition of the thiol ligands like mercaptopropionic acid, thioglycolyc acid or glutathione [28]. This decomposition, leading to a metal sulfide shell, can be assisted by UV-irradiation. Typical examples are CdTe/CdS and ZnSe/ZnS [29, 30].

Adding the shell precursors during the core nanoparticle synthesis can formally be considered as a single-step variant of the described two-step synthesis. The idea behind this approach is to promote the sequential growth of the core and shell materials by carefully adjusting the reaction conditions. In particular, the core and shell precursors have to be chosen in a way that they exhibit a difference in reactivity. Nonetheless this method favors the formation of graded or alloy structures rather than of systems with an abrupt core/shell interface. Examples using this single-step approach comprise highly luminescent InP/ZnS [31] and $Cd_{1-x}Zn_xSe_{1-y}S_y$ nanocrystals [32] or Co NPs coated with a Au shell achieved by heating the Co particles in 1,2-dichlorobenzene, under reflux, with $[(C_8H_{17})_4N]^+[AuCl_4]$ containing trioctylphosphine (TOP) as a stabilizer and the core-shell structure was formed by a process of redox transmetallation between $Co^0$ and $Au^{3+}$ [33].

*2.1.2. Cation exchange*

In contrast to method 1), the shell material is generated at the expense of the core, by replacing the cations in the ionic crystal lattice. As a consequence, the overall nanoparticle size and shape are essentially maintained thanks to the anion sublattice, while the effective core size shrinks. In contrast to bulk materials, the exchange kinetics are much faster in the case of nanocrystals, making it possible for many reactions to take place even at room temperature [34]. The cation exchange reaction is driven by a large excess of the incoming cation and/or the preferential solvation of the outgoing cation. Formation of a more stable crystal lattice can be an additional driving force. The cation exchange method is of particular interest for the growth of heterostructures, which show a large lattice mismatch and there-

fore difficulties for the direct shell growth. Typical examples are PbS/CdS and PbSe/CdSe core/shell nanocrystals [34, 35]. Furthermore, complex heterostructures can be maintained during several subsequent cation exchange reactions, as for example illustrated by the transformation of a CdSe/CdS via Cu2Se/Cu2S to ZnSe/ZnS spherical core / elongated shell (dot in rod) structure [36]. On the other hand,better mechanistic understanding is still needed to enlarge this approach to other materials families. However, the observed mild reaction conditions, fast reaction times and the possibility to generate metastable heterostructures already demonstrate the potential of cation exchange as a powerful tool in the synthesis of novel core/shell systems.

### *2.2. Physical route*

#### *2.2.1. Solvent-free fabrication of core/shell nanoparticles*

In contrast to the numerous processes developed in the liquid phase, comparably small number of solvent-free methods have been investigated to engineer such nanoarchitectures.

Chemical vapor deposition (CVD) is a well known technique to grow not only epitaxial semiconductor core/shell structures but also core/multishell nanoarchitectures. For example Lauhon *et al.* used CVD to grow core/multishell nanowire heterostructures [37]. These authors used a gold particle as a catalyst to grow a semiconducting nanowire using the appropriate gaseous reactant, Figure 1a,b. Then by subsequently introducing different reactants and/or dopants and tuning the experimental conditions to favour homogeneous vapour-phase deposition on the nanowire surface by introducing different reactants and/or dopants, the authors succeeded in producing

core/multishell wires, Figure 1c,d. Si-Ge and Si-Ge-Si core/shell nanowires created using this method are presented in Figure 1e,f.

While CVD is a clean method well suited to the growth of semiconductor core/shell materials [37, 39], different methods have to be developed for other systems such as metals. Habas *et al.* have shown that metal nanocrystals can be used as seeds for growing a metal crystalline shell [40]. Although the growth of the shell was done in the liquid phase, the concept can also be used in vacuum without any solvent. Various differently-shaped nanocrystals and NPs have been grown in vacuum after deposition of metal atoms on metal, semiconducting or insulating substrate surface. The subsequent diffusion of atoms of other species on top of the nanocrystal is expected to lead to the formation of core/shell structures.

Carbon cages can also be engineered in vacuum after deposition of metal atoms onto amorphous carbon thin films at elevated temperature. Transmission electron microscopy reveals that in the case of nickel, the metal atoms form a core and then the carbon atoms of the substrate diffuse on the Ni core to form a multi-layer graphene shell, Figure 1 [38]. Interestingly experimental data show that the graphene layers are growing inwards at the nickel-graphite interface. Carbon shells have also been engineered when Ni particles were heated in close proximity of $C_{60}$ molecules [41].

The fabrication of core metal/shell structures in vacuum appears to be more problematic. The main drawback of depositing metal directly onto supported particles or nanocrystals is the shadow effect, i.e the side of the particle facing the evaporator is coated but it is usually not the case of the particle back side. For example the metal film evaporated onto silica

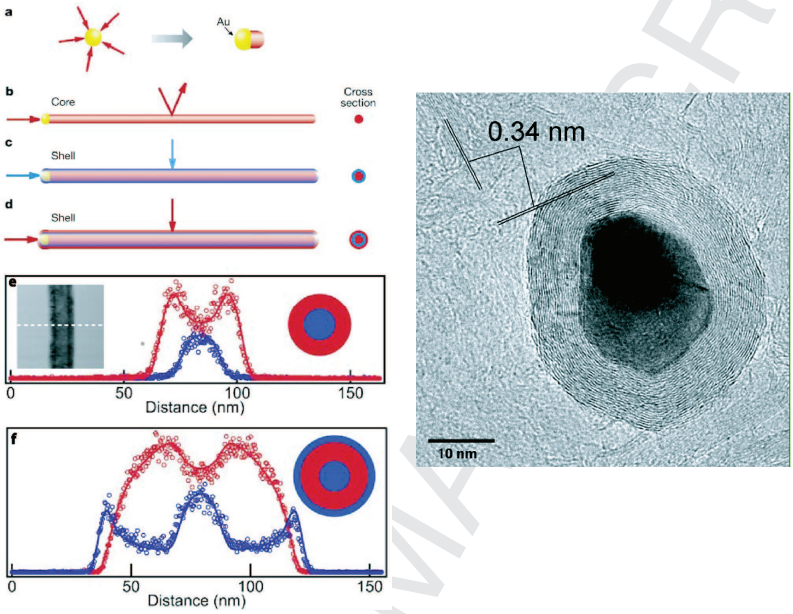


Figure 1: (left panel) Scheme of CVD growth of core/shell nanowires. (a) A gas, the reactants in red, reacts with the surface of a gold nanocluster, the catalyst. This leads to the directed growth of a nanowire (b). (c) When conditions are altered, the the reactant decomposes on the nanowire surface, leading to the formation of a uniform shell (blue). (d) Subsequent modulation of reactants leads to the growth of multiple shells . (e) Inset: TEM image of the Si-Ge core/shell nanowire. Nanowire cross-section indicates a 21 nm diameter Si core (blue circles), 10 nm Ge shell (red circles) and $< 1$ nm interface. (f) Si-Ge-Si core/shell nanowire cross-section shows a 20 nm diameter silicon core, a germanium inner shell (thickness, 30 nm), and p-type silicon outer shell (4 nm). Silicon is represented y blue circles and germanium is represented by red circles [37]. (right panel) Ni particle encapsulated by a graphite shell [38].

spheres on glass was only covering half of the spheres forming a half-shell [42]. The silica spheres can also be coated with a half-shell Ti/W film using the same process. Subsequent deposition of gold on the particles followed by an annealing at 700°C leads to the dewetting of the gold film and the formation of gold microcrystals on the surface of the spheres [43].

Sweeney *et al.* developed an elegant strategy to circumvent the shadow effect occurring during metal coating [44]. They fabricated bottom pyramidal shell using sequentially phase-shifting photolithography, etching, e-beam, and lift-off. First they made cavities in Au-Ti-coated Si(100) substrate. The cavities were then coated with a gold layer (25 nm thick). Silica ($SiO_2$) or polystyrene (PS) particles were then deposited in the cavities. The particles could be molten or not at high temperature to create different structures. Then a 25 nm Au layer was deposited using e-beam on top of the particle to complete the formation of the core/shell particles (see Figure 2). The substrate was then etched in order to release the core/shell particles. The whole sequence is illustrated in Figure 2 along with scanning electron microscopy images on these core/shell structures.

An alternative method for engineering metal core/shell structures consists in the subsequent deposition of metal atoms on surfaces. For example Rusponi *et al.* [45] have grown hexagonal Pt islands on a metal substrate in vacuum after deposition of 0.2 monolayer of Pt at 130 K followed by annealing at 760 K. The cobalt island outline was achieved after subsequent deposition of 0.2 monolayers of Co at 220 K, see Figure 2 a. 2D Pt particles surrounded with Co rim were thus created but not yet supported 3D core/shell systems, i.e. the top surface of the Pt islands was not covered with

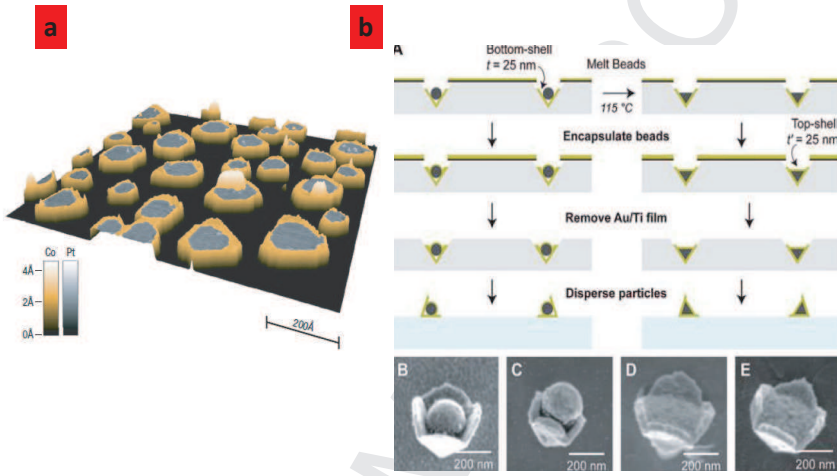


Figure 2: a (left panel) Fabrication of core/shell particles. (A) Assembly of PS or $SiO_2$ beads into pyramidal bottom shells, encapsulated with top shells, and then released to form pyramidal core/shell particles. (B, C) SEM images of Au-PS-Au particles with separated bottom and top shells because of swelling by the PS beads under e-beam deposition. (D, E) SEM images of Au-$PS_{melt}$-Au particles with flat dielectric surfaces covered by a top shell [44]. b (right panel) 3D STM image of Pt islands (gray) surrounded by a single Co atom large crown [45].

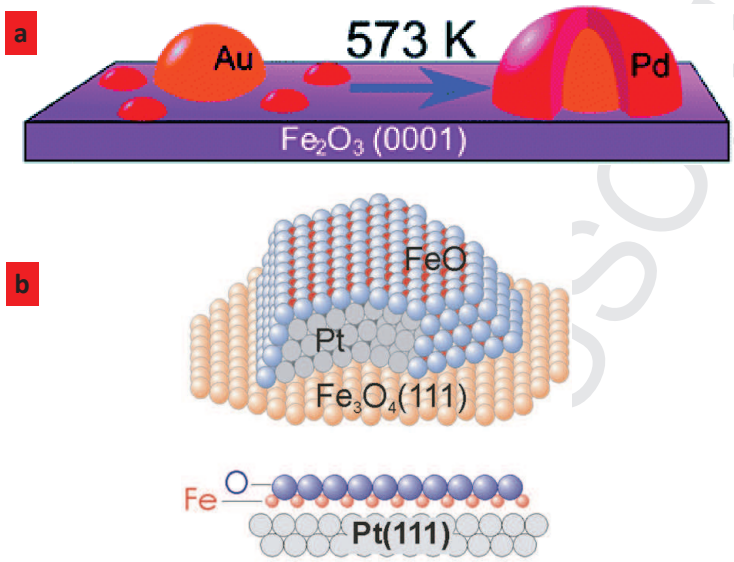


Figure 3: (a) Method to fabricate Au@Pd core/shell NPs on $Fe_30_4$ surface. (b) Scheme of Pt nanocrystals encapsulated with a FeO(111) layer [47].

a Co layer.

Davies *et al.* improved this method to grow core/shell particle on oxide surfaces [46]. They sequentially deposited gold and palladium onto a $\gamma$-$Fe_2O_3$(0001) substrate in ultra high vacuum by metal vapor deposition. The two metals form distinct Au and and Pd particles on the oxide surface. Then the authors claimed that annealing this system at 573 K for 1 minute induces the diffusion of the Pd atoms on the Au particles and then leads to the formation of Au@Pd core/shell particles of few nanometer size. This method is illustrated in Figure 3a.

Metal nanocrystals or nanoparticle encapsulated within an oxide thin film can also be fabricated after depositing metal on an oxide substrate followed by annealing at high temperature. Pt nanocrystals encapsulated within an FeO(111) monolayer have been created after deposition of Pt on $Fe_3O_4$(111) followed by annealing at 850 K, Figure 3b [47]. In a similar way Pd nanocrystals grown on $SrTiO_3$(100) surface are encapsulated within a TiO(111) monolayer after annealing at 900 K [48].

*2.2.2. Gas phase synthesis*

In the family of physical methods for the synthesis of NPs, gas phase synthesis methods are interesting because they offer a continuous way of NPs production and are therefore easily scalable. For example the Flame Spray Pyrolysis is developed at industrial scale. In this method, NPs are synthesized in a combustion flame in a gaseous flow and are collected in a filter placed downstream. Such methods have been implemented and are able to produce core/shell NPs in a simple way, the core is classically synthesized in the first reaction zone while the shell is added in a second reaction zone as shown in Figure 4

In this example [49], oxide NPs of $LiFePO_4$ are synthesized by flame pyrolysis and coated in an oven by decomposition of ethylen with a rate of 7g/hour. A limitation of this method is the production of oxide cores, it can be overcome by the laser pyrolysis method that recently demonstrated the synthesis of Si@C NPs as shown in Figure 4 [50]. In both cases, the NPs were synthesized as elements of Li Ion batteries able to work at high capacity with improved cyclability.

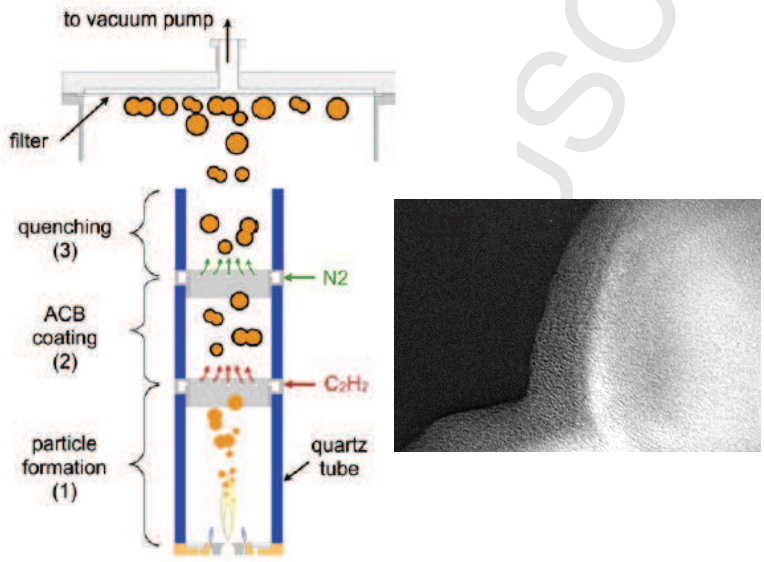


Figure 4: (left panel) Schematic diagram of the experimental setup for the production of $LiFePO_4@C$, $LiFePO_4$ is produced by combustion and coated by carbon in a second reaction zone. The particles are collected after leaving the reaction zone in a flow of neutral gas after the reference [49].(right panel) Si@C core/shell NPs synthesized by laser pyrolysis in a reactor composed of two successive laser-reactant interaction zone. The Si core is synthesized from laser decomposition of silane and coated in a second reaction zone by laser decomposition of ethylen.

*2.2.3. Preformed clusters in the gas phase*

Ligand-free clusters well defined both in size and composition are currently produced in free phase by nucleation in a seeded beam. Among them, laser vaporization source is widely developed. A target is ablated by a pulsed Nd:YAG laser creating a plasma. The plasma is cooled by a continuous flow of a buffer gas (He, Ar) triggering the formation of nucleation embryos. The formation of the NPs is obtained by accretion of the plasma species during a subsequent adiabatic expansion ( $10^8$ K/s cooling rate) [51]. The expansion occurs when the mixture flows through a micrometer nozzle separating the nucleation chamber at high pressure from the deposition chamber at low pressure. The advantage of the deposition of clusters with low energy is that they survive on the substrate essentially without fragmentation, and with little deformation [52]. For binary structures, a target pellet is made by the sintering of a mixture of the two elements. Even though clusters are produced in a non steady state, free survival clusters are close to the equilibrium shape and governed by the segregation rule [53]. Another versatile method has been first proposed by Hoshino *etal* [54] who prepared $Na@Co$ clusters. The clusters are produced in a dual-target dual-laser vaporization cluster source, which allows producing binary clusters. By tuning the delay time between the two laser pulses, and then the embryo formation, A/B and B/A core/shell structures can be prepared [55, 56]. Compared with other existing methods for the generation of core/shell NPs, this method can be applied to a wider variety of materials. However, the method is limited to a low quantity of matter.

## 3. Experimental methods for the characterization of core/shell nanoparticles

Different experimental techniques are especially adapted to the characterization of core-shell structure and its interface.

### *3.1. Transmission Electron Microscopy TEM*

The transmission electron microscope allows not only for the observation of NPs but also the determination of quantitative information, like strain or chemical composition at the nanometer scale. This information is correlated with physical macroscopic measurements. The developments of quantitative electron microscopy have been possible through technical improvements among which are electron guns (working generally at 200kV or 300kV), electron detectors and aberration correctors. For the latter, the image spherical aberration correctors allow for improved spatial resolution and reduction of the interface delocalization [57] whereas the probe correctors reduce the probe size to measure chemical information at the atomic scale. This chemical information can be extracted from three different detection systems corresponding to different physical interactions. The high angle annular dark field microscopy (HAADF) gives a contrast depending approximately on the square of the atomic number $Z^2$ [58]. The exact interpretation of the HAADF images requires however image simulation (figure 5a). The EEL (electron energy loss) and EDX (energy dispersive x-ray) spectroscopies correspond to the inelastic scattering of fast electrons with atoms in the nanoparticle. The fast electrons loose energy that is measured with an EEL spectrometer and spectra give information on the chemistry of the materials, like chem-

ical composition [59] or oxidation degree, and also on optical or magnetic properties[60]. The material can be de-excited through x-ray emission that is measured by dedicated detectors [61]. EDX spectra provide information on the atom present in the NPs but the detailed electronic structure is not available due to the poor energy resolution and detection efficiency compared to EEL detectors.

The correction for the spherical aberration is mandatory to get the atomic resolution in both imaging and chemical analysis of inorganic nanoparticles. For soft matter, it is however necessary to correct also for the chromatic aberration that will limit the resolution at low voltages (below 80kV). The use of low voltage microscopy is more and more widespread to limit the effect of beam damages on the samples.

One aspect of the recent progress of electron microscopy concerns the study of the growth of particles inside the microscope. In a gaseous atmosphere, a dedicated pumping system is added around the objective lens or special sample holders allow for the gas injection inside a reactor [62]. The nanoparticle growth can also be observed in liquid cells where the reaction is initiated by an electron or a photon pulse [63]. More and more experiments are also proposed to study the samples "in operando", the aim is to follow the evolution of the sample under magnetic, optical or electrical solicitations. For the evolution of the magnetic configuration, many techniques in a TEM are available among which the electron holography has proven its efficiency on NPs [64].Study on NPs benefit from all the technical and experimental developments in TEM for some years now, for structural and chemical aspects but also for the determination of local physical properties.

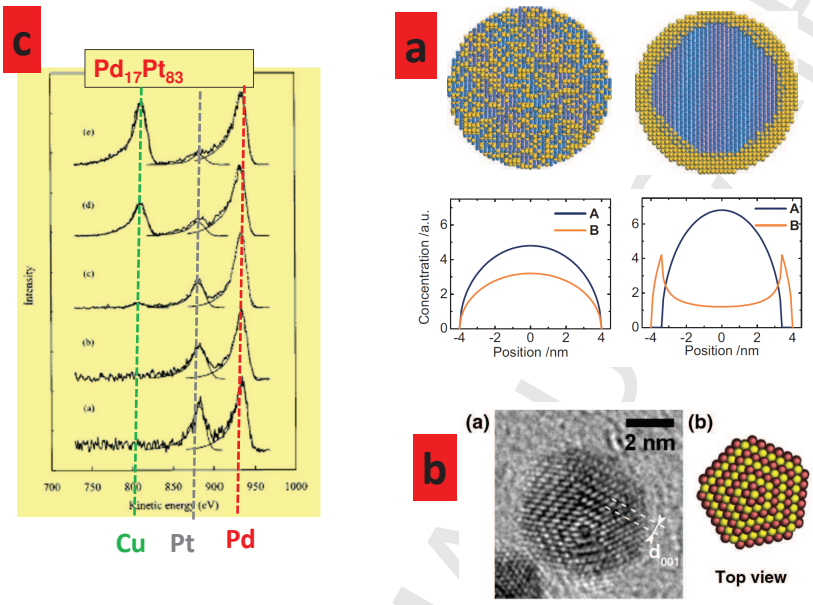


Figure 5: some examples illustrating the observation of a core/shell structure. (a) ideal observation of a core/ shell structure by HAADF. (left) Cross-sectional view of a core/shell NP, (right) in a homogeneous alloy. The HHADF signal gives the concentration of the two materials, A and B, across the equator- ial plane of the particle (left) and (right), respectively (after the original figure of Xu and Wang [65]. Experiemental observations are well illustrated in this paper on figures 16,20, 21 and 22. (b) HRTEM image of a FePt particle displaying simultaneously a fivefold symmetry and L10 ordered domains with a schematic view of the corresponding chemically ordered decahedral structure, predicted by theoretical calculations. In this case the alloying is perfect (after the original figure of Tournus *et al* [66]. (c) Evolution of the LEIS signal during the $^4He^+$ 1-keV ion bombardment of a $Pd_{65}Pt_{35}$ sample after (a)=75 s, (b)=210 s,(c)=660 s, (d)=1335 s and (e)=2235 s sputtering time. The Pd and Pt signals are located at about 870 and 920 eV. The copper signal comes from the Cu substrate. At the onset, no Pt signal is observed indicating that Pt is in the core. During time exposure, Pd atoms located in the outer shell are evaporated revealing Pt atoms in the core (after the original figure of Rousset *et al* [67]).

*3.2. (cryo)-Tomography*

The TEM techniques described in the previous part suffer from the transmission process that induces a projection of the whole sample on a single plane (figure 5b). The NPs are projected in a two-dimensional image and the three dimensional information is lost. Some techniques are available to investigate the $3^{rd}$ dimension, such as electron tomography and atom probe tomography. Several techniques have been developed in the field of electron tomography [68]. The classical one consists in the acquisition of series of images for various tilt angles and the reconstruction of the object through software calculations. The various angles are obtained by tilting the sample holder (monocrystals) or by looking for samples with different orientations (particles). The signal is usually recorded with an HAADF detector [69]. A second method is the discrete tomography method, that necessitates a small number of acquisition but requires the knowledge of the particle structure. This method is based on the fact that the HAADF signal recorded for each probe position is proportional to the atomic number and to the number of atoms in the column. Associated with statistical analysis and the acquisition along 3 different crystallographic axis, the 3D structure of silver particles in an aluminium matrix has been demonstrated on an aberration-corrected STEM [70]. Other reconstruction algorithms, as "compressed sensing" are also studied with the idea of reconstructing a 3D image with few 2D images [71]. Using electron tomography, atomic columns can be imaged in plane but the depth of field cannot reach the atomic resolution along the optical axis.

The atom probe tomography is a combination of field ion microscopy, time-of-flight mass spectrometry and position sensitive detector. Historically,

most atom probes have used a voltage pulse to field evaporate atoms from the specimen. The samples are prepared as needles to enlarge the electric field at the tip and extract the atoms that are analyzed by the mass spectrometer. The study of conductive samples was spread to oxides or semi-conductors with the use of laser pulses focused on the tip. The 3D chemical image is reconstructed using dedicated software, in which various parameters have to be set. Complimentary microscopy analysis can be used, in particular HRTEM and STEM analysis to get these parameters.The screening distance of the electric field at the specimen surface determines the depth resolution. It is usually around 0.1 nm in conductive materials, the atomic resolution being achieved along that direction. Gold NPs embedded in a MgO matrix have been studied by atom probe tomography, making it possible to determine the composition of individual particles [72].

### *3.3. EXAFS, XPS*

Among the many techniques linked to x-ray radiation available to analyze materials, absorption techniques and surface photoelectron spectroscopy will be detailed as they are the most commonly used. X-ray absorption spectroscopy techniques (XAS) are used to study the structure of materials, by studying the local structure around selected atoms. XAS experiments are sensitive to chemical species and can be applied on materials without long-range order, making this technique unique among spectroscopy techniques. In x-ray absorption spectroscopy, the information comes from the transition of occupied levels to unoccupied valence orbitals. In XANES (X-ray Near Edge Structure), the absolute position of the edge contains information about the oxidation state of the absorbing atom. Its shape gives information on

the vacant orbitals, electronic configuration and site symmetry of the absorbing atom. In EXAFS (Extended X-ray Absorption Fine Structure), the oscillatory part of the absorption coefficient above a major absorption edge can indicate the number and species of neighbour atoms, their distance from the selected atom and the disorder (thermal or structural) of their positions. The interpretation of the oscillations requires the use of *ab-initio* calculations. Commonly installed on synchrotron lines, the XAS experiments can be combined with a deposition chamber to follow the growth process of materials.

X-ray Photoelectron Spectroscopy (XPS) probes the bonding energies of electrons by the analysis of the kinetic energy of the emitted electrons after an irradiation under monoenergetic x-ray photon beam (in the 200eV-4000eV range). If the incident energy is sufficient, a core electron will be ejected to the vacuum. Each chemical element is characterized by a spectrum with different peaks corresponding to different orbitals, from which the oxidation state of the material can be deduced [73]. The peak intensities depend on photoionization cross section and the comparison of the peak areas provides an quantitative analysis of the chemical composition. The position of the peaks can indicate some chemical shifts, keeping in mind that the energy reference is crucial in this kind of experiments [74]. The XPS experiments is limited to the analysis of information on the sample surface because of the short inelastic mean free path for electrons. This length is on the order of a few nanometers and depends on the material. In the case of core/shell nanoparticles, XPS using synchrotron radiation of variable energy enables to distinguish between core/shell and alloy nanoparticles even in the case of very

small dimensions ($< 5nm$) [75]. When lower energy photons are used to probe the surface, the spectroscopy is called UPS (UV photoelectron spectroscopy), the photon energy is in the 10-45 eV range. This spectroscopy is used to probe filled electron states in the valence band or adsorbed molecules on metal. By detecting photoelectrons at different emission angles, the energy of the electrons as a function of the momentum vector may be determined. This process is known as "band mapping" and is a powerful probe of the electronic structure of crystalline materials. The distinction between UPS and XPS is becoming less and less well defined due to the continuous energy range available with synchrotron radiation.

### *3.4. Low energy ion scattering*

Low Energy Ion Scattering technique (LEIS) is a powerful probe for segregation studies. Unfortunately, this method classified as destructive remains little known despite its high selectivity in depth profile and sensitivity [52, 67]. LEIS is a surface-sensitive technique that selectively probes the outermost atomic layer and is therefore well adapted to the study of surface segregation. A beam of monoenergetic (energy $E_0$ about 1keV ) $He^+$ ions of mass $M_1$ is focused on the surface of interest. Some of these ions are backscattered from the surface through an angle $\theta$ and their energy distribution is analyzed. The intensity of the LEIS signal is mainly assigned to the collisions involving the first atomic layer (figure 5c). The position of the elastic ion peak is given by the simple relationship assuming hard sphere model

$$\frac{E}{E_0} = (\frac{M_1}{M_1 + M_2})^2[\cos\theta + [(\frac{M_2}{M_1})^2 - \sin^2\theta]^{1/2}]^2 \quad (1)$$

where $M_2$ is the mass of the surface atom involved in the collision. The same equation is valid for a binary compound. Note that E gives through $M_2$ measurement the nature of the atom. At the onset, the superposition of two signals ($M_2$ and $M_2^{'}$ masses) in the backscattering energy spectrum is related to alloying, one signal being related to a pure shell. The intensity calibration is done with reference samples (single crystals with different orientations). Since a low sputtering is observed, a depth profile can be obtained as a function of time.

## 4. Core/shell nanoparticles: specific advantages arising from the heterostructure

### *4.1. A rapid survey*

Core/shell structure refers to a multilayered particle which is the result of core and shell division where the core is totally surrounded by the shell (onion-like structure)(figure 6). This is a particular case of total segregation in an alloyed particle. Total segregation leads to two classes of multilayered particles Janus and core/shell type. The main difference between the core/shell particles and the Janus particles (dedicated to Janus in roman mythology, a two-faced god looking in the future and the past) is the morphological features of their components mutual arrangement, where there is only one of them on the surface of core/shell NPs. These Janus NPs have different properties (such as charge, polarity, optical or magnetic properties) at opposite sides while core/shell NPs have properties arising of those of the core or the shell. Their combination can also give rise to novel properties, not achievable with the individual materials alone. Core/shell NPs can be

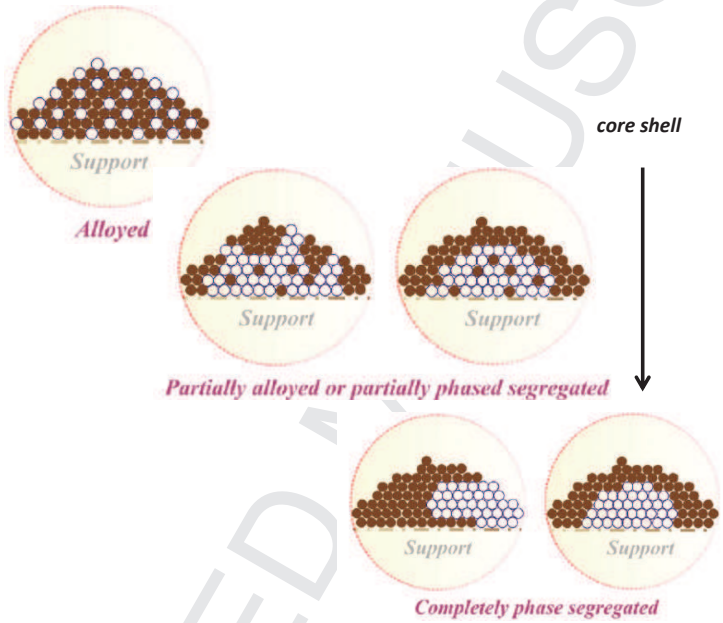


Figure 6: Some examples illustrating different configurations in a binary system. The completely phase segregated has two forms: a core/shell (right) and a Janus form (left) after the original figure from Wanjala *et al* [76]

classified in two groups according to the role of the shell:

-shell as core protection

This is well illustrated in Co/X or Fe/X (X coinage metal) where the non reactive metal at the surface of the magnetic nanoparticle is a suitable protecting tool [10]. The magnetic property is related to the core as long as no polarization effect or sizeable electron transfer is observed.

-"smart shell" with targeted properties

We only consider the case where the shell contributes to the passivation of the core surface suppressing surface trap states without noticeable alteration of the electronic properties. Jeon *et al* [77] reported the synthesis of metallic Mg nanocrystals embedded in a gas-barrier polymer matrix(PMMA) that enables both the storage of a high density of hydrogen and rapid kinetics with applications in fuel cells batteries (Figure 7). This core/shell structure illustrates well the selective coating which protects the core from the oxidation and which is permeable to the hydrogen migration.

Likewise, Lee *et al* [11] studied $ZnO/TiO_2$ NPs produced by the sol-gel method for batteries. In this case, the $TiO_2$ avoids the migration and the dissolution of Zn in the electrolyte, $TiO_2$ remaining a transparent barrier for ion migration ($TiO_2$ has high ionic conductivity and is very resistant to corrosion). This is well illustrated by the low softening of the discharge capacities against cycle number (figure 8).

Coating of iron oxide NPs with a gold shell was initially proposed as

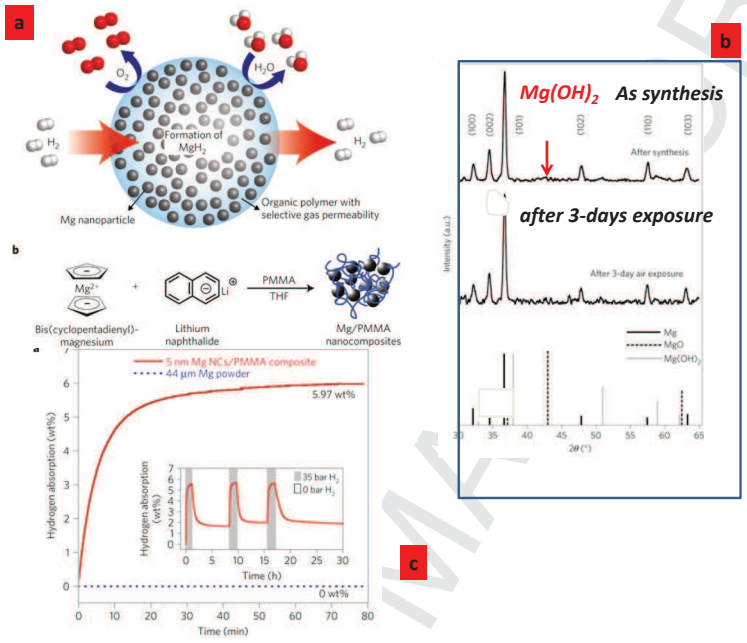


Figure 7: Mg NPs in a gas-barrier polymer matrix. (a) Schematic of Mg NPs encapsulated by a selectively gas-permeable polymer with a synthetic approach to formation of Mg NPs embedded in PMMA nanocomposites. (b) The diffraction pattern reveals pure Mg without alteration after an long time exposure (3 days at air). This illustrates the coating efficiency with a no sizeable ($Mg(OH)_x$) contribution (the expected diffraction peaks in oxides are displayed).(c) enhancement in hydrogen absorption properties of $Mg@PMMA$ composites (absorption at $200^oC$ and 35 bar of $H_2$) in comparison to bulk powder Mg. The maximum of hydrogen absorption is reached after one hour, the value is close to the theoretical one (7.6%). The stability is also observed by the reversible absorption-desorption cycle (after the original work from Jeon *et al* [77])

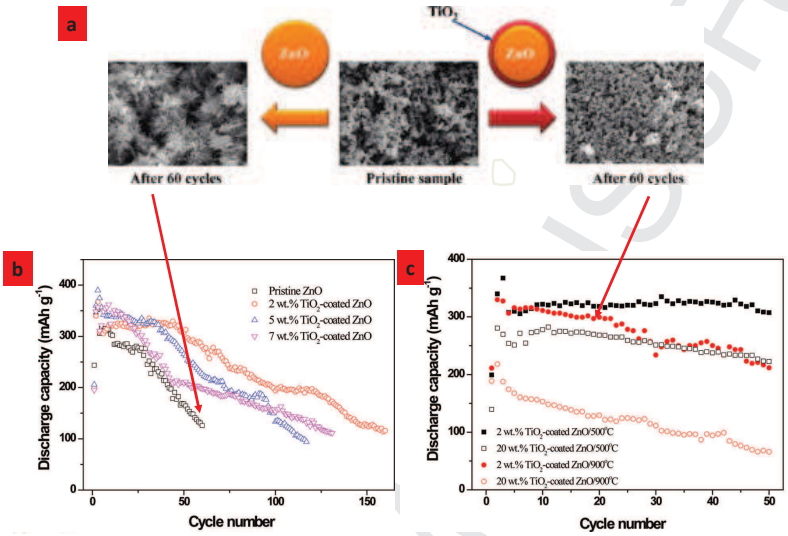


Figure 8: Discharge capacities of pure ZnO pristine, 2, 5, and 7 wt % $TiO_2$- coated ZnO and (b) discharge capacities of 2 and 20 wt % $TiO_2$-coated ZnO annealed at 500 and 900 $^oC$. At low temperature ($< 500^oC$) $TiO_2$ is in anatase structure. Above $500^oC$ a transition towards rutile phase is observed and corresponds to an enhancement of the protection. At this stage a core/shell structure is expected. At high temperature $700^oC$ and above, a partial alloying with $ZnTiO_3$ and $Zn_2TiO_4$ phases is reported especially in Ti-rich compounds. This corresponds to a lower efficiency with the lack of the core/shell structure. The morphology of the $ZnO@TiO_2$ electrodes is also given after 60 cycles. The dendritic forms observed in pure pristine exhibits the dissolution and recrystallization of zinc atoms during the electrochemical process (after the original work of Lee *et al* reference [11] .

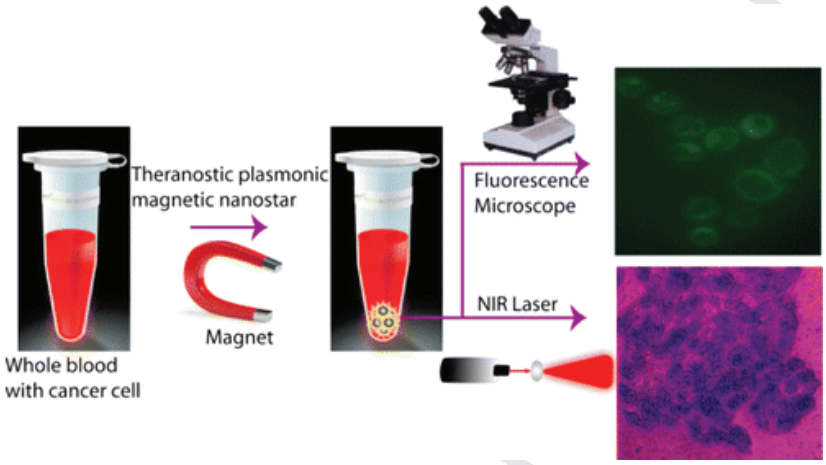


Figure 9: Schematic representation showing the separation, fluorescence imaging and photothermal destruction of cancer cells using magnetic@plasmonic NPs (from reference [82].

a strategy to protect their spontaneously oxidizable surfaces and provide a surface for chemical functionalization [78, 79]. The ability to combine the magnetic and optical properties of the composite material opened new perspectives for biomedical applications. To this aim, complex structures such as iron oxide/silica/Au NPs or star-shaped iron oxide/gold NPs were engineered, simultaneously enabling multiple functions such as MRI imaging, magnetic guiding and NIR photothermal therapy (figure 9) [79, 80, 81, 82, 83, 84].

*4.2. Hollow structures*

Among core/shell structures, hollow nanocrystals [85] offer applications in nanoelectronics, nano-optics, drug delivery systems, and as building blocks for lightweight materials. Even though the chemical route is the standard procedure for hollow structure synthesis [86, 87], a physical route based from the conversion of solid to hollow NPs known as the "nanoscale Kirkendall effect" was successfully investigated [88]. The Kirkendall effect is the motion of a boundary layer between two elements that occurs as the consequence of the sizeable diffusion rates between the two elements at high temperature. Caruso *et al* [89] showed that the thickness of the hollow sphere as well its size and shape can be readily controlled during growth. A new class of core/shell NPs with the core lying in a hollow cavity opens an alternative way to tune the coupling between the optical features of both metal and non-metal counterparts. While solid Au/CdSe/CdS core/shell/shell NPs do not show any fluorescence, a fluorescence signal albeit with low quantum yield (0.8%) is observed for hollow core/-shell NPs after etching CdSe by dilute $H_2O_2$ (Figure 10) [90]. The increased fluorescence of hollow NPs versus solid ones presumably results from a decrease of the density of CdS surface trap states due to a mild oxidation by $H_2O_2$. Furthermore, a weakening of the quenching effect induced by the Au core could contribute considering that the distances between Au cores and some parts of CdS increases due to the movement of the cores in the rattle structures after CdSe removal.

Another example of the tunability offered by hollow cavity between the core and the shell is given by $Au/Cu_2O$ NPs [91] (fig. 11). The engineering of the light absorption and scattering was achieved by a fine-control of geo-

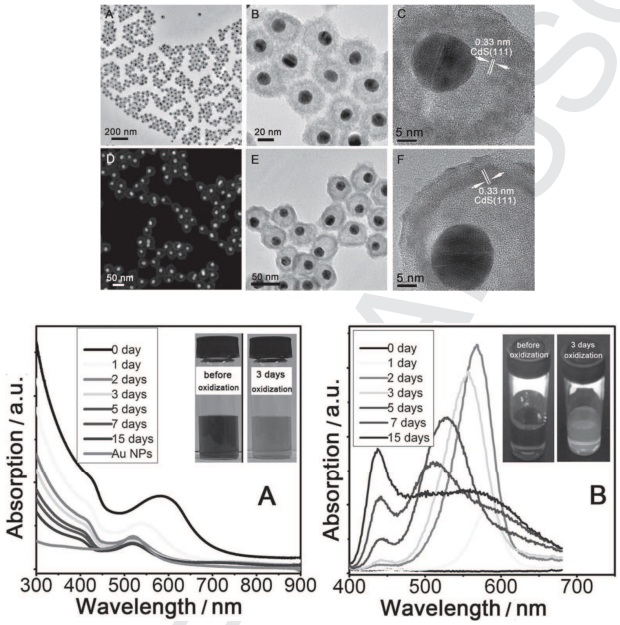


Figure 10: Transmission electron microscopy images of Au@CdS nanostructures after etching of CdSe by dilute $H_2O_2$ for 7 days (A-C) and 15 days (D-F). The overall sizes are 44 nm. The fluorescence spectra of Au@CdSe@CdS hollow NPs are shown A) UV-vis and B) for different oxidation time (from the reference[90]).

metrical parameters, such as $Cu_2O$ shell thickness, size of the Au core, and the spacing between the core and shell. Finally, selective ion diffusion can be used for the elaboration of novel core/shell structures, which do not contain obligatorily a cavity. An example is the transformation of $\epsilon$-Co nanoparticles into Co/Co-P core/shell structures containing an amorphous cobalt phosphide shell [92]. This intermediate structure is obtained by inward P diffusion preceding the complete transformation of $\epsilon$-Co into $Co_2P$ nanoparticles through subsequent outward Co diffusion accompanied by Kirkendall hollowing.

*4.3. Self focusing in solid state reactions*

In classical nucleation theory, the radius (hence the surface/volume ratio) is of prime importance. The capability to change the surface energy through the net concentration of A (core) or B (shell) atoms at the surface offers a new degree of freedom. Then, core/shell structures can be used to monitor nucleation and growth with a self focusing effect (figure 12). Radmilovic *et al* [12] prepared the ternary compound Al-Sc-Li with a core of $Al_3(Sc; Li)$, incorporating both Sc and Li on the B-site sublattice of the $L_{12}A_3B$ structure and a $Al_3Li$ shell. They found a remarkably uniform distribution of core/shell precipitates with $L_{12}$ structure (such binary compounds $Al_3X$ type intermetallic phases crystallizes in the $L_{12}$ structure) even though without size selection (figure 12). However, the self focusing in the nucleation growth requires drastic conditions on temperature range, phase diagram, diffusion factor and solubility (trend to alloying) of each element in the final compound. The self focusing regime is reached when $\frac{\partial^2 r}{\partial t^2} < 0$ ( $\frac{\partial r}{\partial t} < 0$ determines the critical radius) reported in nucleation growth in colloidal solution. Even though,

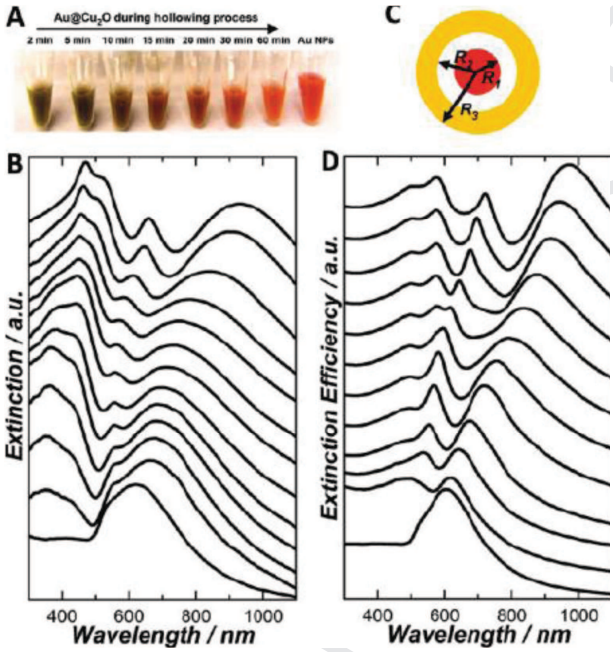


Figure 11: Optical tunability of $Au@Cu_2O$ NPs. (A) Photograph of colloidal suspensions with an average $Au@Cu_2O$ outer radius of 130 nm obtained at different reaction times during the symmetric hollowing of $Cu_2O$ shells. The right-most sample is bare Au colloids. (B) Experimentally measured extinction spectra of colloidal suspensions of $Au@Cu_2O$ NPs obtained at different reaction times: 2, 5, 10, 15, 20, 25, 30, 40, 50, 60, 75, and 90 min (from top to bottom). The bottom spectrum is corresponding to bare Au colloids. (C) Geometry of $Au@Cu_2O$ employed for Mie scattering theory calculations. (D) Calculated extinction spectra of a $Au@Cu_2O$ with fixed R1 of 63 nm, fixed R3 of 130 nm, and varying R2 of 64, 65, 66, 68, 70, 75, 80, 86, 93, 100, and 110 nm (from top to bottom). The bottom curve is the calculated spectrum of a spherical Au nanoparticle (63 nm in radius) (after the reference [91]).

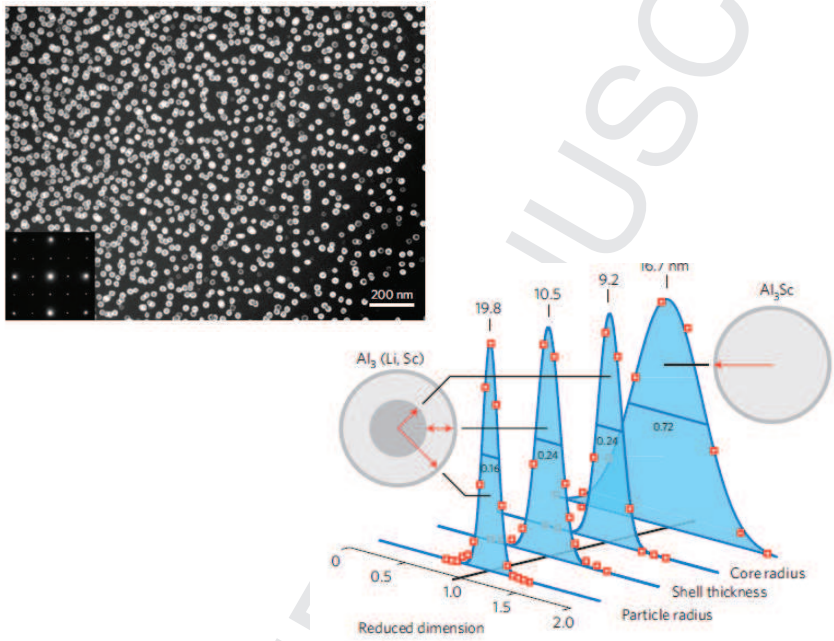


Figure 12: Size distributions of core/shell AlLiSc NPs measured with dark field TEM showing an uniform distribution of core/shell precipitates with $L_{12}$ structure(see the weak reflections of the $L_{12}$ superlattice in the Fourier transform (in insert). The strong reflections correspond to (100) crystal orientation. The size distribution is shown in the right part compared to the broad distribution of $Al_3Sc$ compound where no self focusing is observed. (after the original figure from Radmilovic *et al*)[12].

severe conditions limit the self-focusing regime, formation of a core/shell nanostructure is a method for in situ size selection during growth.

### *4.4. Beyond surface protection: application to catalysis*

Now, let us consider the case where the shell modifies the electronic properties. It has been shown that it is possible to tune the physical properties in a larger window than that of each constituent taken separately by the appropriate choice of the core and shell materials. This opens a new field of tailored nanomaterials with high selectivity and high sensitivity especially for catalysis or plasmonic applications.

#### *4.4.1. Metal catalysts*

Turkevich and Kim [93] introduced a very important concept of catalysis using two different metals such as Au and Pd in the same nanoparticle. Core/shell nanostructures are a convenient way to integrate multifunctionality into the electrocatalysts of metallic NPs. Catalysts are often expensive. At a first glance, in NPs of catalyst metal, the center atoms are burried and cannot take part in reactions. A core/shell particle can be constructed in a way that the catalyst atoms are located only on the outside (the shell region), while the core can be constituted by a catalytically inactive low-cost material. This structure has the advantage in that all the catalyst atoms can take part in reactions. In this case, the core does not play a significant role excepted for the shell growth. This crude assumption holds for large shell thicknesses when the core atoms are totally embedded and located far away from the surface. In other words, the core atoms do not introduce a perturbation (polarization, electron transfer) as long as the thickness of the shell is

large (typically few angstroms) as compared to the Thomas Fermi screening of the core atom into the shell medium. For applications, electrocatalysts need to be highly active and durable under harsh reactive environments. It is therefore advantageous to protect the catalyst with another element. Sekol *et al* [94] synthesized Ag/Pd catalyst NPs supported on multi-walled carbon nanotubes for use in fuel cells. The new catalysts are highly active and alcohol-tolerant for oxygen reduction reactions (ORR) in alkaline media. For the smallest ones where the shell is very thin, the core atoms are partially exposed and can serve as catalytic active sites. Core/shell structures can be used to engineer materials with tailored properties, concerning polarization, delocalization, hybridization or massive electron transfer between core (shell) and shell (core). This is the key point for the enhancement of catalytic activity [95]. Very recently, Qi *et al* [13] reported an enhanced catalytic activity of core shell $Au/CeO_2$ NPs compared to $Au-CeO_2$ having a Janus form (Au deposited onto $CeO_2$). In addition, these authors found a remarkable stability upon CO oxidation (figure 13). The key point is the interfacial bonding between the core and shell which can alter the electronic structure with an enhancement of the net activity and stability [96]. Note that both effects are antagonist since a good activity requires a thin protection film (shell) while a good stability requires a large capping. The ideal compromise is probably with one monolayer as suggested by Hwang *et al* [97]. However, this is a pure illusion since for uncomplete shell, the adatoms occupy preferentially either under coordinated or over coordinated sites at the surface.

A very promising application of the core/shell nanostructure is the concept of bifunctional systems where two reactions are monitored within the

same nanoparticle [98]. For example, Ni/Ru NPs have been demonstrated to act as a bifunctional system for the hydrolysis reaction of ammoniaborane and also for magnetic separation [99]. For fuel cell applications Chen *et al* [100] proposed a bifunctional catalyst where the core (oxides) material catalyzes an oxygen evolution reaction whereas the shell (nitrogen doped carbon fibers) material catalyzes an oxygen reduction reaction. This field of application is very promising, because in full rise for the realization of selective and efficient effects in catalysis science.

*4.4.2. Oxides catalysts*

In the context of environmental and energy shortage concerns, photocatalyst efficient for air and water treatment by decomposition of organic pollutants and water splitting for hydrogen production are subjects of intense research activity. Due to its good chemical stability, weak toxicity and low cost, $TiO_2$ is the most used oxide photocatalyst but several limitations must be overcome. $TiO_2$, as many photocatalyst, is active mainly under UV light, leaving apart a large part of the solar spectrum. Therefore many studies are dealing with the engineering of the bandgap (stoichiometry, insertion of heteroatoms ...) in order to shift the absorption towards the visible range. In the photocatalysis process, an electron-hole pair is created under excitation. Ideally, the electron and the hole are separated and the activity is due to the reaction of external chemical species with the charges when they reaches the surface of the nanoparticle (figure 14 top). However, the recombination of charges before their separation is a major loss mechanism. In this context, synergistic effects expected from coupling metal nanostructures with oxide materials, in a core/shell architecture, appear especially interesting in the

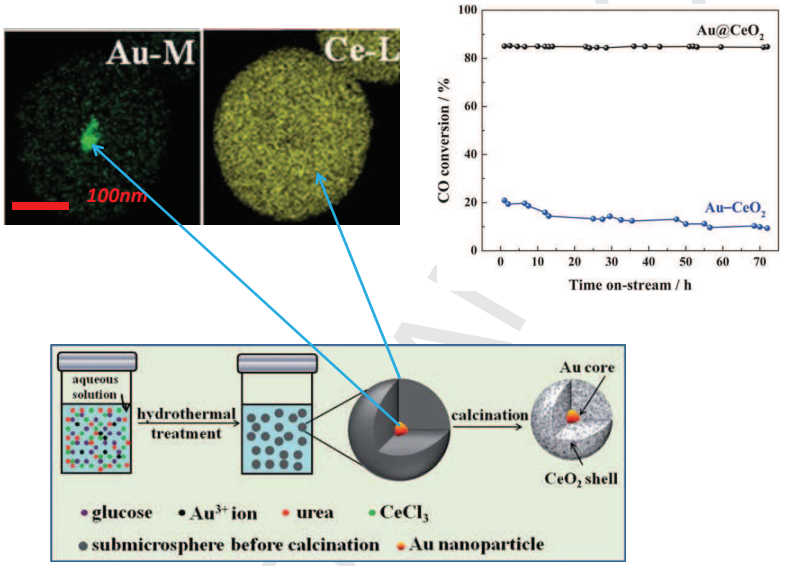


Figure 13: Schematic illustration for the synthesis of $Au@CeO_2$ NPs with the core/shell structure via the hydrothermal method. The use of cerium cation and its low hydrolysis ability in water or alcohol solution does not allow sol gel process. HAADF-STEM mapping image of one nanoparticle shows the repartition between gold located in the core surrounded by cerium atom. The CO conversion against time of $Au@CeO_2$ core/shell versus $Au - CeO_2$ mixture assimilated to a Janus form well illustrates the gain in efficiency and stability in core/shell structures. (after the original figures from Qi *et al* [13])

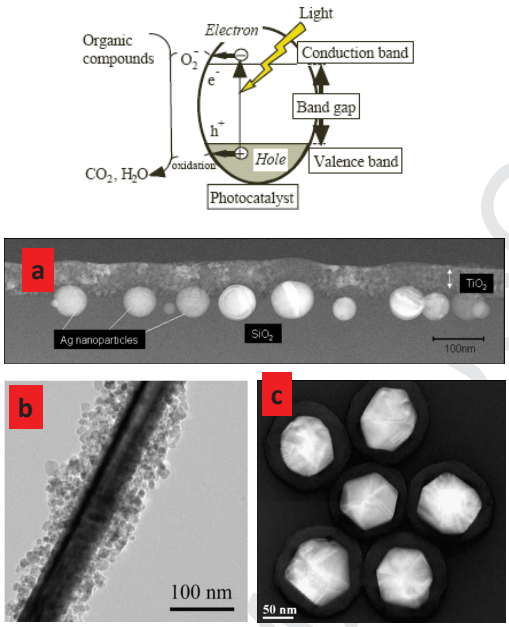


Figure 14: top: mechanism of photocatalysis available on the site http://www.tipe.com.cn/library/kb2502.htm. Bottom: Various morphologies of core/shell nanostructures elaborated from photocatalysis applications, (a) Ag surrounded by $SiO_2$ in a $TiO_2$ layer (after the reference [101], (b) Ag nanowires coated by $TiO_2$ NPs (after the reference [102], (c) Ag@C NPs (after the reference [6]

field of heterogeneous photocatalysis (or photovoltaics) by addressing these two key points: enhancing the efficiency of photocatalysts by decreasing losses due to charge recombination or enhancing light absorption especially in the visible range by taking advantage of the surface plasmon resonance (SPR) of some metallic particles.

Among many possible examples, a typical organization is a metallic core embedded in a semiconductor (SC) shell such as M/SC with in most cases

M = Pd, Pt, Cu ... or Au, Ag ... with various geometries (from spherical NPs to nanowires, Figure 14-bottom illustrates some Ag based core/shell structures) and SC= $TiO_2$, $SiO_2$, CdS, C ... In the core/shell architectures, $TiO_2$ remains the most used semiconductor. From the point of view of visible absorption, Ag/AgX (X=Br, Cl) exhibits good properties, due to SPR of Ag NPs [103] and are efficient photocatalyst under visible irradiation. However, in many publications as can be seen for example in the review paper by Wang [103] the activity is tested using dyes such as Methylen Blue. Even though such tests are defined in the ISO international standard, such experiments are no longer considered as pertinent models for testing photocatalysts (due to phosensibilisation effects)and/or only the total activity under light with at least a UV contribution is tested [101, 102].

The efficiency of Ag@C was tested for the decoloration of RhB under visible light and interestingly for the degradation of acetaldehyde under visible light. The degradation of acetaldehyde is followed by the measurement of $CO_2$ concentration but the authors do not precise how they discriminate from the $CO_2$ naturally evolving from Carbon structures [104]. An original structure composed of a $SiO_2$ core, decorated by gold NPs and with a non metallic doped $TiO_2$ shell has been synthesized and tested with very good results for the degradation of a dye and dichlorophenol under visible and sunlight irradiation [91]. Few studies contain, as the latter one, both information: behavior under UV irradiation together with behavior under visible light and comparison with a standard [91]. Therefore it is not easy to achieve conclusion about efficiency of mechanism under visible excitation. In $M/TiO_2$ nanocomposites, the activity can be improved in the visible range

but a decrease is often observed in the UV range and is attributed to the lower light absorption [105].

## 5. Semiconductor/semiconductor core/shell structures

### *5.1. Compound semiconductors, type-I vs. type-II structures*

The growth of a semiconductor shell gives the possibility to precisely engineer the band gap and energy levels and hence the optical and electronic properties of semiconductor nanocrystals. The most extensively studied systems are heterostructures showing a type I band alignment. In this case the smaller band gap core material is encased within a larger band gap shell material (Fig.15top). The shell acts as a potential barrier and spatially confines the exciton within the core. Therefore the photoluminescence wavelength remains essentially unchanged, while its quantum yield can be strongly increased, due to the improved passivation of surface defect states by the shell. In addition, the photo-stability can be greatly enhanced if a chemically inert shell material is used. The most well known examples are CdSe/ZnS, CdSe/ZnSe and InP/ZnS [14]. In type II systems, the core and shell materials exhibit a staggered band alignment (Fig. 15 top). Here, the lowest energy states for the charge carriers of the exciton are localized in either the shell or the core, respectively. The spatial separation of the charge carriers also leads to a lower effective band gap than that of the core and the shell material. Therefore type II systems can be used for shifting the emission spectral range to larger wavelengths. The first reported type II quantum dots were CdTe/CdSe whose emission wavelength could be shifted from 670 to 1000 nm by adjusting the core diameter and shell thickness [106]. The

same work also presented CdSe/ZnTe nanocrystals, which are an example of an inverted type II structure, showing photoluminescence up to 900 nm.

Strain induced by the lattice mismatch of the two crystallographically different materials, can potentially induce defects that can be detrimental for the emission properties. The lattice mismatch in the family of Cd- and Zn-chalcogenide core/shell systems for example ranges from 0.4% (ZnTe/CdSe) to 19.8% (CdTe/ZnS). However, in contrast to bulk heterostructures, strain can be more easily absorbed by colloidal nanocrystals owing to their small size and large surface curvature. Strain exerted by the shell can lead to compression or dilatation of the core. The resulting change of the inter-atomic distances modifies the conduction and valence band energy levels. Among the II-VI semiconductors, CdTe is particularly prone for large volume changes due to its low bulk modulus of 42.4 GPa. Smith *et al* [4] tuned the band alignment of CdTe/ZnSe nanocrystals (lattice mismatch 14.3%) from type I to type II with increasing shell thickness . Using a 1.8 nm CdTe core, a giant shift in the emission wavelength from around 520 to 870 nm was observed upon growth of 6 ZnSe monolayers. This shift is accompanied by a gradual decrease of the optical absorption features and a marked increase of the photoluminescence lifetime from 18.4 ns for a 3.8 nm CdTe core to 115 ns after growth of 6 ZnSe monolayers. Against initial expectations, type II core/shell nanocrystals can show very high fluorescence quantum yields as demonstrated for CdTe/CdSe (82%) [108] and ZnSe/CdSe (85%) [109]. In the latter system, the continuous transition from (inverted) type I to type II and back to type I behavior has been observed when increasing the CdSe shell thickness on a 3 nm ZnSe core (Fig. 15-bottom) [107].

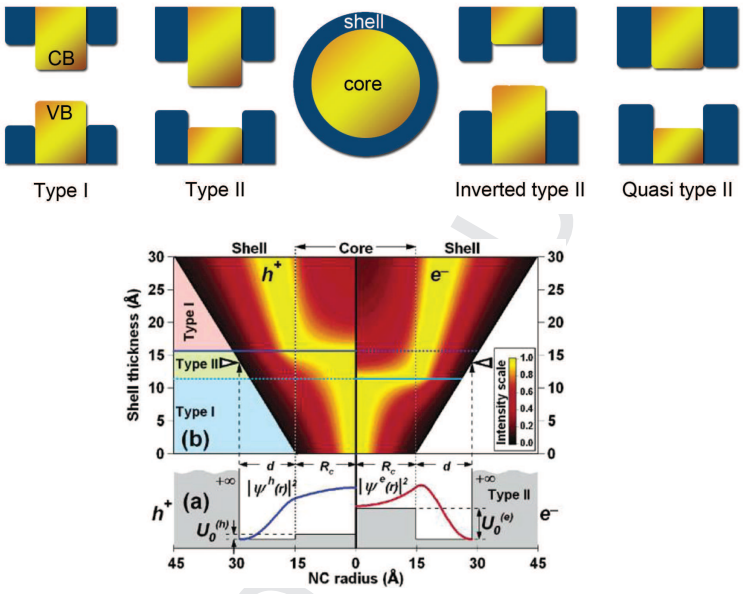


Figure 15: top:Scheme representing the main types of energy band alignment, which have been realized in core/shell nanocrystals (VB: valence band, CB: conduction band). Bottom: ZnSe/CdSe core/shell nanocrystals. a) Representation of the valence (left) and conduction (right) band diagram and radial distribution of hole and electron density functions calculated for a 3 nm ZnSe core covered with a 1.4 nm thick CdSe shell. b) Radial distribution of the hole and electron density functions for variable shell thickness d on a 3 nm core. Reproduced with permission from Ref.[107] Copyright American Chemical Society 2004.

Fig. 15-bottom also shows another type of band alignment occurring for some material combinations, named "quasi type II", and characterized by the absence of an energy step between the conduction (or valence) band edges of the core and shell semiconductor. In such a case, the hole (electron) is confined in the core whereas the electron (hole) wave function diffuses in the shell. The most prominent example here is CdSe/CdS, showing an emission wavelength shift on the order of 40-90 nm during shell growth [26]. At the same time, the relatively low lattice mismatch (4%) in this core/shell system allowed for growing very thick shells of 15-20 CdS monolayers leading to diameters approaching 20 nm, while maintaining significant fluorescence [110, 27]. Importantly, a large fraction of these "giant" core/shell nanocrystals does not show the characteristic fluorescence intermittency ("blinking"), which is ubiquitously observed for semiconductor quantum dots and other types of organic and inorganic fluorophores. These results suggested that the thick shell strongly reduces the probability of nanocrystals' ionization by trapping one of the carriers in surface states. Indeed, in a charged nanocrystal, the extra charge induces non-radiative Auger recombination, which occurs on a faster timescale (10-100 ps) than radiative recombination (several ns). The charged nanocrystal is in a dark "off"-state.

Adding one or more shell materials on the surface of core/shell nanocrystals gives additional degrees of freedom in terms of band gap engineering. Core/shell/shell systems have first been introduced with the goal to use an intermediate CdS or ZnSe shell as "lattice mismatch adapter" in the widely studied type I system CdSe/ZnS [111, 112]. In the meantime this strategy has been extended to the formation of core/shell structures with a compositional

gradient. In a recent example, a fluorescence quantum yield of 100% has been reported for green emitting CdSe-ZnS alloy nanocrystals, covered with a graded CdSZnS shell [113]. The remarkable progress in chemical synthesis of core/shell systems also opens the door for the design of so-called quantum dot/quantum well (QDQW) structures. Here a material of lower band gap is embedded between a core and an outer shell of a larger band gap material. This structure is particular suitable for the 3D wavefunction engineering and has first been realized in the aqueous synthesis of CdS/HgS/CdS nanocrystals [114]. By judicious choice of the materials, such onion-like structures can even show several distinct emission features: Battaglia *et al* [115] reported an inverted QDQW by covering a red-emitting CdSe/ZnS core/shell structure with a CdSe shell, which gave rise to an additional green fluorescence peak. Spherical core/anistropic shell structures constitute another important class of semiconductor/semiconductor core/shell nanocrystals, which have attracted much attention due to their distinct optical and electronic properties. Prominent representatives are CdSe (spherical dot) / CdS (elongated rod) shell structures [116, 117], for which the so-called seeded-growth method developed by Manna and coworkers [118] led to an unprecedented control of size and shape. These nanostructures have been used, for example, in combination with silica microspheres on whispering-gallery-mode resonators to demonstrate single-mode, spectrally tunable lasing [119]. Achieving optical gain without using external resonators is however still a challenging task, due to the competing detrimental process of Auger recombination. In the case of semiconductor nanocrystals this process is highly efficient when they are in the multi-exciton regime, i.e. at higher pumping energies.

In this respect, CdSe/CdS core/shell structures are of particular interest: Auger recombination is strongly reduced as a consequence of the reduction of spatial confinement of the excited carriers, presumably caused by alloying at the core/shell interface [120]. Among more complex anisotropic semiconductor/semiconductor core/shell structures CdSe/CdS tetrapods [121], CdSe/CdE (E:S, Se, Te) octapods [122], CdSe/CdS "dot-in-plate" (spherical core, disk-shaped shell) [123] and ZnE/CdS-Pt (E=Se, Te) dots in rods heterostructures comprising a Pt seed at one end [124] can be found. The latter exhibit interesting photocatalytic properties for hydrogen production.

### *5.2. Group IV element semiconductors derived from fullerenes*

Fullerenes and onions like structures are widely reported as exotic forms of carbon with a nearly $sp^2$ hybridization. Many studies have been reported for silicon carbide because of its promising technological applications. In the bulk SiC, Si and C atoms bind through $sp^3$ type bonding. However, it is well known that in standard conditions, Si atoms are $sp^3$-hybridized (diamond) while carbon atoms prefers $sp^2$ forms (graphite). It is possible to separate both hybridizations in a core/shell structure. In this case, atoms exhibit $sp^3$ bonding when in the (3-D) core and $sp^2$ bonding when in the (2-D) shell. Using silicon in the core and carbon in the shell, yields a specific hybridization-assisted segregation effect, where each component (Si and C) adopts its preferential hybridized state. These (expected) structures called buckydiamonds [125] or fullerene onions [126] have already been reported in pure carbon structures with a coexistence between bucky diamond, nanodiamond and fullerene carbon phases according to the number of atoms in the particle [127].

## 6. Oxide core/shell nanostructures

Insulating materials, as bulk materials, are widely used for their optical or magnetic properties in particular because they can be easily and strongly doped with many interesting elements (rare-earth, transition metals ...). The downsizing of such materials generally allows the possibility to increase even more the doping concentration. The use of core/shell structures adds an additional degree of freedom that can be put in use to either demultiplicate the properties of a single nanoparticle or to create new properties that are not attainable either in bulk or in one-component nanostructures.

### *6.1. Up conversion of photoluminescence*

A first example of the extension of property by a core/shell structure is the possibility to tune the upconversion observed in some insulators over a broad range of excitation and/or emission wavelengths.

Upconversion is the ability for a given material to transform two or more absorbed photon in the IR into a visible or UV photon. This process is very efficient in systems doped with Ytterbium and either Erbium or Thullium for which $Yb^{3+}$ acts as the IR absorbing element while $Er^{3+}$ or $Tm^{3+}$ are the emitters. The first advantage of upconversion is the fact that since the excitation is at longer wavelength than emission most fluorescence from contaminants or surrounding media is suppressed. A second interesting point is that the process is orders of magnitude more efficient than two photon processes thus accessible with very simple light sources (CW laser diodes for instance). But the drawback is that only a limited number of systems show a good efficiency. It has been recently shown that the core/shell approach

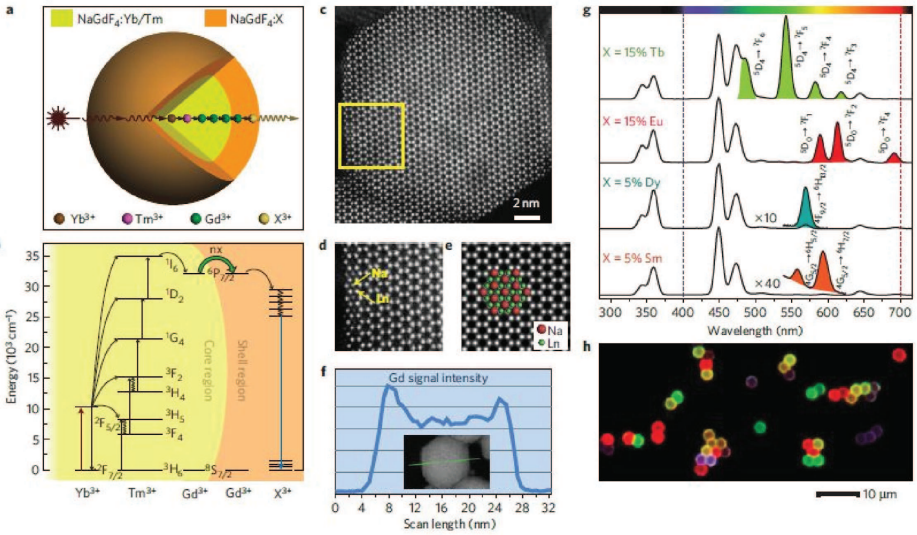


Figure 16: (a) schematic design of the core/shell structure, the center part is codoped with $Yb^{3+}$ and $Er^{3+}$ ions, the first shell is undoped $NaGdF_4$. The external shell is doped with the desired rare earth ion $X^{3+}$. (b) scheme of the energy levels involved in the process. (c) HRTEM of one particle (d) and (e) zoom of the HRTEM image showing the rare earth ions and the sodium ions. (f) EDS signal of the gadolinium ions. (g) some examples of the upconversion luminescence observed as a function of the rare earth ion inserted in

can suppress this drawback [128].

By designing a core/shell structure it is possible to physically separate the excitation from the emission. In part (a) of figure 16 is shown the design of the core/shell system developed by Wang and collaborators [128]. A classical up conversion system : $NaGdF_4$:$Yb^{3+}$,$Tm^{3+}$ constitute the core of the particles. It is surrounded by an undoped $NaGdF_4$ shell in which gadolinium ions will act as excitation carriers as illustrated in part (b) of the figure. The excitation can be carried away over tenth of nanometers to a second shell in which any fluorescing ion having levels below the $^6P_{7/2}$ energy level of gadolinium can be excited and give rise to luminescence as evidenced in part (g) of the figure. This is also true for molecules close enough to the particles and even some charge transfer between particles can be observed. The combination of this two recent approaches open-up new possibilities for the use of up converting particles in many different applications: in imaging for biology of course but also for photodynamic therapy [129, 130, 131, 132] or for photovoltaics [133].

### *6.2. Luminescence and magnetism for imaging*

Core/shell structures also allow the multiplication, on a single nanoscopic platform, of different properties [134, 5, 135, 136]. This possibility has been widely explored for the combination of luminescence and magnetism in particular for the different and complimentary imaging techniques these two properties allow.

### *6.3. Core/shell magnetic oxide for biomedical and data storage applications*

Concerning magnetic nanomaterials, the core/shell architecture is a way to independently address the competing technical demands on the magnetic

properties, such as the thermal stability of magnetization and coercivity. Such structuration is promising to improve the energy product of permanent magnets and in enhancing the thermal stability of magnetic nanocrystals to overcome the "superparamagnetic limitation" in recording media. Some of the significant and most promising applications for inorganic magnetic NPs (NPs) lie in the fields of biology and biomedicine. A major issue with the development of inorganic NPs for biological applications pertains to the stability and size of biofunctionalized NPs in biological media and also to the development of inorganic cores with enhanced or multifunctional properties. Core/shell structures are the current investigated and most promising way to ensure such multifunctionalisation. Among inorganic coating strategies for biomedical applications, coating of metallic oxide NPs with silica [19, 137, 138, 139, 140, 141, 142, 143] has been largely developed as well as with Au and other metals or metal oxides. A silica shell is the most common approach for protection and modification of magnetic cores. It can prevent any direct contact of the magnetic core with additional reagents to avoid unwanted interactions, such as acidic corrosion. Furthermore, silica coatings have many advantages such as better biocompatibility, better stability under aqueous conditions (hydrophilicity), developed and facile surface modification approaches, and easy control of interparticle interactions [144, 145]. Furthermore dye molecules or other compounds can also be co-encapsulated into the silica shell allowing combining optical imaging [19, 141]. The core/shell structuration of magnetic metallic oxides by combining materials with different magnetic properties is a way to finely tune the nanoscale magnetic properties (fig. 17). Thus a significant increase in the efficiency of magnetic

thermal induction (hyperthermia) by NPs has been obtained by taking advantage of the exchange coupling between a magnetically hard core and magnetically soft shell to tune the magnetic properties of the nanoparticle and maximize the specific loss power, which is a measure of the conversion efficiency [24]. The optimized core/shell magnetic NPs have specific loss power values that are an order of magnitude larger than conventional iron-oxide NPs. An antitumour study in mice has been performed and the therapeutic efficacy of these NPs was found to be superior to that of a common anticancer drug (doxorubicin).

Such bimagnetic (hard/soft or soft/hard) core/shell nanocrystals have also been demonstrated to be a valid design to separately control the blocking temperature and the coercivity in magnetic nanocrystals by varying the materials, their combination, and the volume ratio between the core and the shell and by switching hard or soft phase materials between the core and shell [146, 20, 147]. Such controls via a bimagnetic core/shell architecture are highly desirable for magnetic nanocrystals in various applications such as magnetic imaging, sensing, drug delivery, and magnetic hyperthermia. A supplementary anisotropy terms is evidenced in metallic oxide core/shell nanostructures involving contacts between a ferro-or ferrimagnetic materials and an antiferromagnetic materials. It is due to exchange coupling between the spins at the interface between the ferromagnetic (FM) and antiferromagnetic (AFM) materials, called exchange bias [148, 149, 150, 151, 152, 153, 154, 155]. The study of FM-AFM exchange interactions proposed interesting development to improve the performance of permanent magnetic materials by means of an enhancement of the coercivity

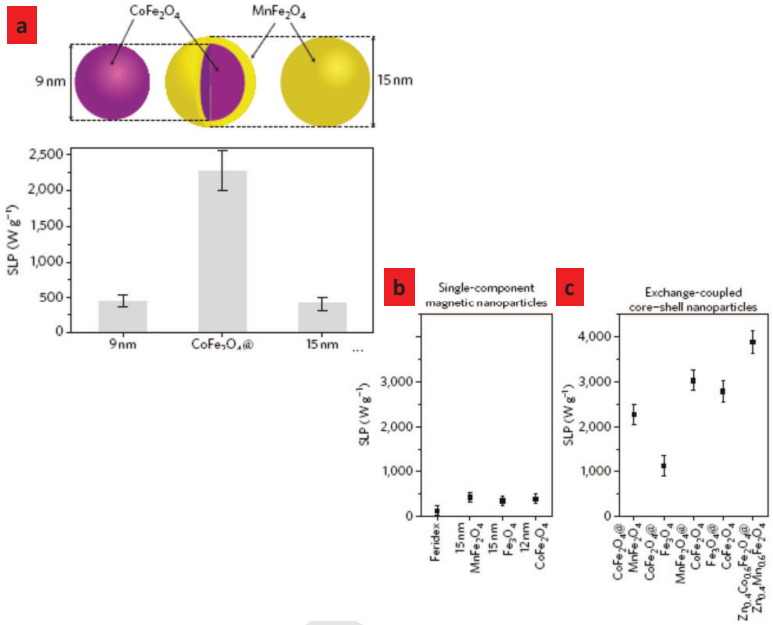


Figure 17: SLP comparison of magnetic NPs. (a) schematic of 15nm $CoFe_2O_4$@$MnFe_2O_4$ nanoparticle and its SLP value in comparison with the values for its components (9 nm $CoFe_2O_4$ and 15nm $MnFe_2O_4$). (b,c) SLP values of single-component magnetic NPs (Feridex and $MFe_2O_4$ M=Mn, Fe and Co) (b) and various combinations of core/shell NPs ($CoFe_2O_4$@$MnFe_2O_4$, $CoFe_2O4$@$Fe_3O_4$, $MnFe_2O_4$@$CoFe_2O_4$, $Fe_3O_4$@$CoFe_2O_4$, $Zn_{0.4}Co_{0.6}Fe_2O_4$@$Zn_{0.4}Mn_{0.6}Fe_2O_4$) (c) SLP values range from 100 to 450 $Wg^{-1}$ for single component magnetic NPs, and values for core/shell NPs range from 1,000 to 4,000 $Wg^{-1}$ (f=500kHz, H0= 37.3$kAm^{-1}$). Error bars indicate standard deviation (n=5). After the original figure and caption reference [145]

which typically accompanies the hysteresis loop shift or to overcome the superparamagnetic limit of NPs. The current change is a deeper understanding of exchange bias in AFM/FIM core/shell nanostructure, which is important for guiding the design and fabrication of magnetic nanodevices for information storage applications. Such magnetic core/shell nanomaterials are also developed with a magnetic metallic core NPs such as $FePt@Fe_3O_4$ [156].

Core-shell NPs ($M_xFe_{3-x}O_4@Au$ or $Au@M_xFe_{3-x}O_4$) with different shapes [157, 158, 159] are also designed in nanomedecine to promote multifunctional NPs [160]. The gold part which may display different shapes such as nanorods may be used for near-infrared fluorescence imaging, for radiosensitization and for the photothermal ablation of cancer cells. The iron oxide part which also may display different shapes may bring imaging (by MRI) and/or therapeutic (by hyperthermia) properties.

## 7. Criteria for the formation of core/shell nanoparticles: case of metals

Core shell structure in nanoparticles is a template of the segregation effect in bulk lattice. A brief review of the basic mechanisms of segregation will be helpful for the following

### *7.1. Structural properties*

In cluster science, excepted so called quantum-size effects, properties are widely related to the surface/bulk ratio and then to the radius in the droplet model. In core/shell structures, the curvature radius plays an important role monitoring the interface between core and shell. We can adopt the same strategy for the interface starting with the infinite surface. Then, surface

segregation, growth mode and strain energy gained at the interface are the key point parameters.

*7.1.1. Surface segregation*

The surface segregation energy is the energy cost of transferring an impurity atom from the core to the surface of a host crystal. In a solid bulk solution, the sign (positive for segregation and negative for chemical ordering) of chemical order can change with the change of A-B alloy composition (i.e. the stoichiometry "$c$" in $A_{1-c}B_c$) and temperature and are related to formation enthalpies (A, B and AB).There are two ways to describe segregation inside a binary compound. The first one is based on the standard Gibbs procedure and requires experimental information concerning phase boundaries and enthalpy of mixing at different temperatures. The second one is based on the phenomenological Landau theory of phase transitions with the so called order parameter [162]. Thermodynamic criterion for segregation in the bulk phase is expressed as

$$|\Delta_{ordering}| > k_B T(c \ln c + (1-c) \ln 1 - c) + \frac{\Phi^2 E}{1-\mu} \tag{2}$$

The first term is the entropic component in the Bragg-Williams approximation. The energy of ordering is positive in the case of the tendency toward phase separation (i.e. core/shell) and negative in the case of the tendency toward ordering). E is the Young modulus, $\mu$ the Poisson's ratio and $\Phi$ the linear strain per unit composition difference. Segregation is widely related to the modification of the electronic structure with T and c. In NPs, the surface plays an important role since energy strain can be relaxed at the surface. Two additional factors, surface energy and steric hindrance, are under

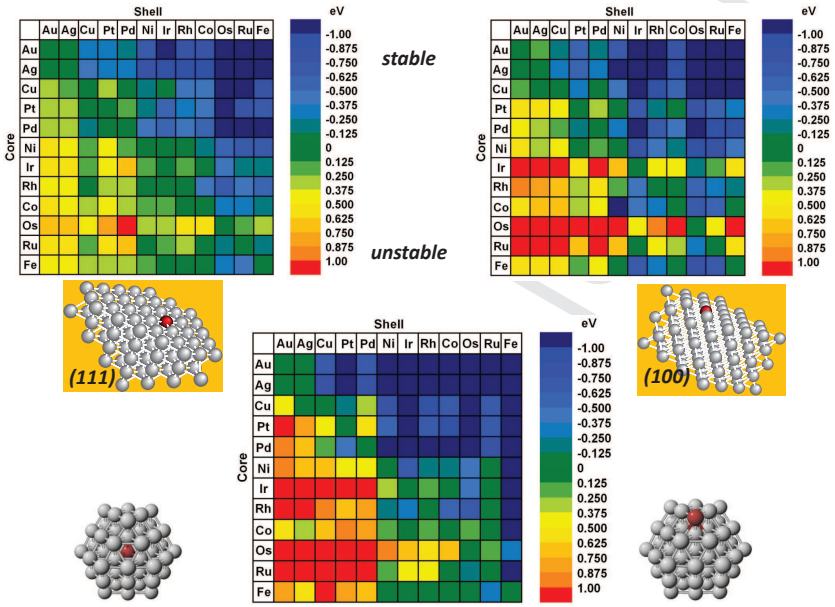


Figure 18: Color-coded matrix of segregation energies for impurity in 55-atom nanoparticle composed of 12 late-transition metals. Elements located around the diagonal have a trend to alloying rather core/shell structure. Color towards blue indicates a stable core/shell structure as depicted in the matrix. Conversely, color towards red indicates that the core/shell structure is reversed. The matrix located at the top are related to (111) and (100) surfaces, the matrix at the bottom is related to the cluster. The ball and stick figure represents the two opposite case (alloying with the atom at the centre and total segregation with the atom at the surface). (after the original figure from Wang and Johnson [161])

consideration. Besides, in bulk phase, at lower temperatures, surface segregation can be limited by the diffusion of atoms from the bulk to the surface or interface. This is not the case at nanoscale where diffusion takes place in low distance. Phenomenological theories incorporate such factors as the heat of solution of alloys, the difference in the pure metal surface energies, and the atom size mismatch in their description of the surface segregation in extended surfaces. This is not enough at the nanoscale where size effects are more or less prominent. In this respect, microscopic theories of surface segregation including tight-binding theory embedded atom method (EAM) and density functional theory are better. Wang and Johnson [161] studied within DFT framework the correlation between elements and segregation between them. Note that strictly speaking, this is a general behavior as long the calculation is done with one atom as impurity corresponding to $c \sim 0$.

Since the degrees of freedom are important in NPs with strong relaxation allowed, the authors found that the segregation energy is larger in NPs because of larger change in coordination number, more relaxation in volume and stronger magnetization in the case of transition metals. Among the main parameters, cohesive energy and Wigner size radius govern the segregation for $c \sim 0$ as depicted on figure 18. Ruban *et al* [163] within DFT-LDA framework stated that for transition metals a simple model based on Friedel's rectangular state-density approximation for surface energies describes the calculated trends in the surface segregation in transition metals quite well. The element with the lowest surface energy will segregate towards the surface. Segregation in NPs is extremely sensitive to the coordination number of the adatoms. Nevertheless, the inspection of the figure 18 suggests

an enhancement of the driving force which governs the segregation effect in a cluster compared to flat surfaces.

*7.1.2. Segregation versus Wullf theorem*

Shape-controlled nanocrystals possess well-defined surfaces [164]. General strategies for high selectivity and efficiency for catalysis requires specific facets. Heterogeneous nucleation (for example the addition of preformed seeds to a metal precursor in the presence of a weak reducing agent [165]) allows a control over size and shape. In core/shell NPs, the segregation is an alternative route for monitoring size and shape. Equilibrium shape in a free particle (monoelement) at zero temperature is given by the Wullf's construction. In fcc metals, it corresponds to the first Brillouin zone namely the truncated octahedron. Wulff construction gives a size-independent thermodynamic shape according to the formula

$$\frac{\gamma_i}{h_i} = Cte \tag{3}$$

The areas of the facets can be obtained by tracing radii in the appropriate direction with a length proportional to the surface energy $\gamma_i$ and a plane perpendicular to the radius vector $h_i$. The minimal polyhedron delimit by the intersection of the innermost planes is the equilibrium shape. This is not true for binary or more complex structures and the equilibrium shape becomes size dependent in the nanoscale regime. The Wulff shape of a fcc nanocrystal is usually determined by its two lowest energy planes, i.e. the {111} and {100} facets. Then the ratio under consideration is $h_{111}/h_{100}$ , for a monovalent fcc crystal this ratio is 0.866 in the basic broken bond model. Ringe *et al* derived the Wullf construction for a binary system where

segregation effect can lower the ground energy with respect to homogeneous alloy. In this case [166]

$$\frac{\gamma_i}{h_i} = K(G) \tag{4}$$

$K(G)$ term contains a new contribution which is the difference in bulk free energy $G$ (defined as the deviation from a linear variation of bulk free energy per unit volume between two pure components) between the true bulk free energy and the expected energy of a perfect alloy with a linear interpolation value for lattice and energy with concentration. The authors consider two classes "weak" ( $\Delta G < 1\%$) and "strong" alloys ($\Delta G > 1\%$). The deviation between the perfect alloying (i.e. no segregation) and the "true" structure is displayed on figure 19 (right panel). This change in the equilibrium shape is of prime importance for the catalysis. Note that the shape can be modified at non zero temperature since shape changes induced by temperature has been already observed and predicted in gold NPs (figure 19 left panel).

*7.1.3. Patchy Multishell Segregation*

The simple segregation with a surface region rich in B element and rich outermost planes in A element is a particular case observed for example for AuNi and PdCu NPs. Usually, complex segregation leading to patchy multishell segregation including, ordering transformation, spinodal decomposition [168] and oscillations, are observed for a given temperature. Hillert and Rundgren [169] gave a simple relationship for segregation within a simple nearest-neighbor interaction model including the enthalpies of the bonds AB, AA and BB and the enthalpies of the broken bonds at the surface. The same behavior is observed in NPs. Barcaro [170] predicted an oscillation in

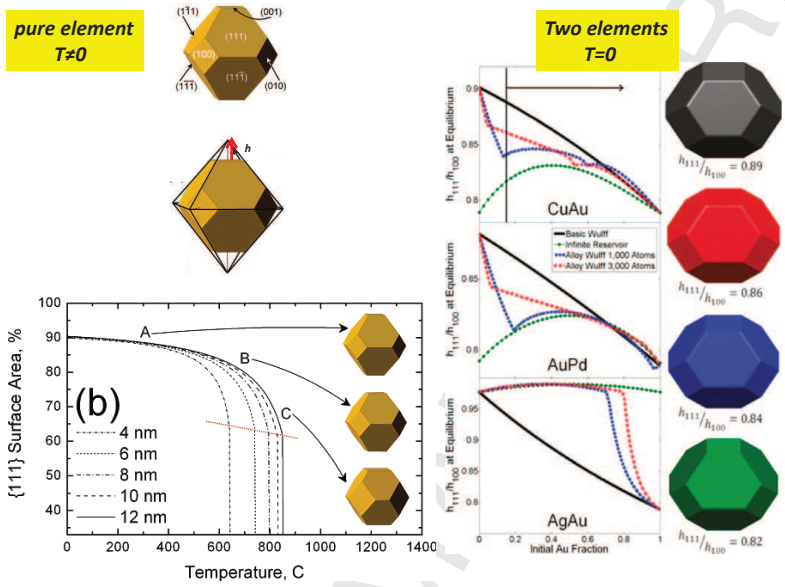


Figure 19: left panel top: calculated Wulff construction (top) and schematic (bottom) showing the parameter h which determines the truncation (ratio between 111 and 110facets). (after the original curve from Barnard *et al* [167] ). right panel: ratio between 111/100 facets at the equilibrium calculated for different models against composition (a) Size and composition dependence of the particle shape computed for a homogeneous alloy (basic Wulff), a segregating alloy with an infinite reservoir approximation (bulk model), and the "true" alloy Wulff mode for N=1000 atoms and 3000 atoms respectively. For N=1000 atoms a total segregation leads to an incomplete core/shell structure. The shape is size-independent for homogeneous and infinite reservoir alloy NPs. The shape dependence for Au fraction of 0.15 is also displayed (after the original figure from Ringe *et al* [166].

small PdPt nanoclusters even though alloying is expected in the bulk phase. Segregation in PdPt has been already experimentally observed by Rousset *et al* [67] . Chepulskii *et al* [171] within Monte Carlo simulations reveal that in PtFe alloy first surface layer Pt segregation is compensated by Pt depletion in the second subsurface layer. Within Modified embedded atom method and montecarlo method Wang *et al* [172] reported three trends in Pt-Re, Pt-Ni and Pt-Mo systems (see figure 19). Starting with the Wullf's form (truncated polyhedron with a magic number of 586 atoms), the authors found a simple core/shell structure in $Pt_{75}Re_{25}$ with the outermost layer platinum rich while, the strong ordering tendency of Pt and Ni leads to $Pt_{75}Ni_{25}$ NPs forming a surface-sandwich structure in which the Pt atoms are strongly enriched in the outermost and third layers while the Ni atoms are enriched in the second layer. In $Pt_{80}Mo_{20}$ NPs, the Pt atoms weakly segregate to the surface. The Pt atoms segregate preferentially to the large coordinated sites (facet) rather than edge and apex sites. The patchy multishell segregation is very important for catalysis since the outer shell composition is strongly related to the cluster size for which very narrow and well defined size distributions are required.

*7.1.4. Core/shell structure versus Janus particles*

The criterion for a surface segregation of one atom ($c \sim 0$) indicates a phase separation but this is not enough to validate a core/shell structure since core/shell or janus type structures can be obtained. The core/ shell structure corresponds to step by step thin film growth according to the Frank-van der Merwe (FdM) process where the deposited atoms B perfectly wets the substrate A. Antithetically, during Volmer Weber (VW) growth, the absence

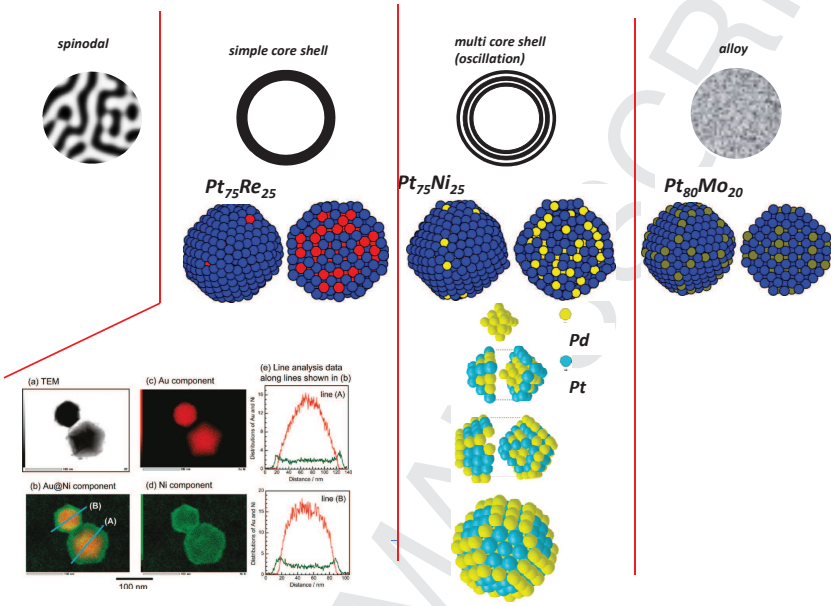


Figure 20: Illustration of different cases corresponding to simple-, multi-core/shell and alloying both theoretically and experimentally. Snapshots of equilibrium $Pt_{75}Re_{25}$, $Pt_{75}Ni_{25}$ and $Pt_{80}Mo_{20}$ NPs containing 586 atoms simulated at T = 600 K: (a) exterior and (b) [0 0 1] cross-sectional views. Pt, Re, Ni and Mo atoms are in blue, red, yellow and dark yellow, respectively. Note that Mo atoms are preferentially in the uncoordinated sites (edges and apex) (after the original figure from Wang *et al* [172]). This is the same behavior reported in PdPt core/shell structure with Pd atoms located at the uncoordinated sites. PdPt presents a muli core/shell structure like PtNi. (bottom, left panel)(after the original figure from Barcaro *et al*[170]). Left panel (bottom): experimentally core/shell structure in Au@Ni showing an Au core and Ni shell. TEM-EDS analysis showing the concentration along the lines A and B (after the original figure from Tsuji *et al* [173]).

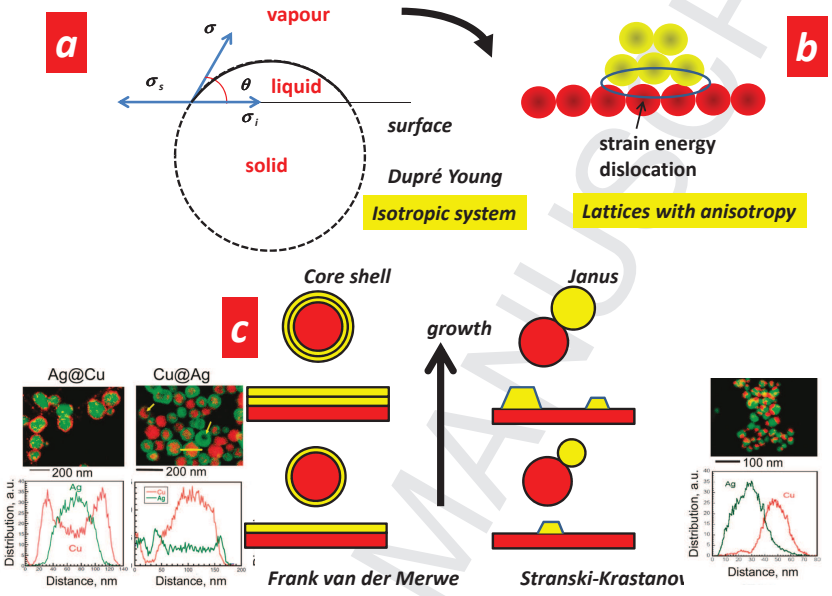


Figure 21: (a) equilibrium shape of a liquid droplet with a curvature radius r deposited onto a structure less substrate. (b) This ideal case is a template for the growth of B nucleus onto A substrate. Due to the anisotropy of the lattice orientation and mismatch, additional parameters (strain energy, misfit dislocation ...) are introduced in the final equation. (c) schematic view illustrating the two opposite growth modes leading to core/shell and Janus structures. The forms are illustrated by three morphologies of Cu/Ag hybrid NPs, prepared by chemical way with different reaction parameters. ) EDX mapping (bottom) and line-scan profile ( top) indicates that the morphology varies from a pure core/shell to a Janus structure. (after the original figure from Cortie *et al* [3] ). The initial work comes from the references [173, 174].

of wetting leads to 3D islands of B atoms mimics the Janus form. When a liquid droplet (B element) on a smooth structure less is considered on a smooth structureless substrate (A element) the shape of the nucleus is given by the Dupré Young relationship (see figure 19 bottom)

$$\sigma_s = \sigma_i + \sigma \cos\theta \tag{5}$$

where $\theta$ is the wetting angle, $\sigma_i, \sigma_s, \sigma$ the interfacial energies between solid and vapour, solid and liquid and liquid and vapour, respectively. The growth of epitaxial thin films on a single crystal surface can be deduced from the previous equation including sursarturation, strain and misfit energies as long A and b atoms have different lattices and orientations. Introducing the difference between B adatom cohesive and adhesive energies $\Delta\sigma = \sigma + \sigma_i - \sigma_s$ through the general formula of Markov and Kaischew [175]

$$\Delta\sigma <> \frac{\Delta\mu - n(\epsilon_s - \epsilon_d)}{2s_c} \tag{6}$$

Where $\Delta\mu$ is the supersaturation defined in the nucleation theory as the difference of chemical potentials of the bulk (B element) and the new phases (A+B elements, A being the core) at the temperature T, n is the number of lateral bonds per atom in the nucleus (2D or 3D), $s_c$ the area occupied by a surface atom,$\epsilon_s$ the homogeneous strain energy per atom and $\epsilon_d$ the misfit dislocation energy per atom. The operator $>$ is related to the condition when 2D nucleation takes place (ie core/shell, FdM surface adhesive force is stronger than adatom cohesive force) while the operator $<$ is related to the condition when 3D nucleation takes place (i.e. Janus, VW adatom cohesive force is stronger than surface adhesive force).

*7.1.5. Core/shell interface*

Because of the curvature, misfit dislocation $\epsilon_d(n)$ and strain energy $\epsilon_s(n)$ are size dependent. In common bulk heterostructures, the misfit stress induced by a lattice mismatch is determined by a curvature analysis. Similarly, the nanoparticle curvature induces or reduces misfit stress. Epitaxial growth is currently observed in $Au@Ag$ [176] and $Au@Pd$ with a low mismatch (0.2%, 4.6% respectively). By contrast no epitaxy is observed in Au@Pt (3.8%). It is generally accepted that no epitaxial growth is observed when the lattice mismatch between the two metals is greater than 5%. However, epitaxial growth with large mismatches are observed for $Au@Cu$ [174] (11.4%), $Au@Ni$ (13.6%) and $Pd@Cu$ [177] (7.1%). The competition between Janus and core/shell in $Pd@Cu$ is well illustrated on the figure 22. At the beginning of the nucleation process, Cu atoms are adsorbing on one or two of the side faces of a seed Pd nanocube leading to Janus's form. The core/shell is formed at the end of the nucleation. The authors explained this two step core/shell formation by the nucleation of preliminary Cu embryos through localized epitaxial growth because of the large lattice mismatch between Pd and Cu. Lattice mismatch has a significant impact on the epitaxial growth of heterostructures. Habas *et al* [40] demonstrated that low mismatch produces conformal shape-controlled core/shell particles while large lattice-mismatch give anisotropic growth with specific shapes. The control of the shape is of importance for catalysis, optical and magnetic applications. This surprising result with epitaxy despite huge misfits underlines the capability for the system to relax constraints at the interface. This is due to additional freedom degrees in a 0D system (i.e nanoparticle) as compared to 2D (i.e. infinite

surface ) system. Nevertheless, EXAFS measurements show for example a compressive stress in Ni@Pd NPs due to Pd atoms in the top layer with larger atomic radius compared with Ni. The large mismatches can be explained templating the large reversible shear strain observed for example in nanowires. Very recently, Wang *et al* [178] reported a reversible shear strain as high as 34.6% in nickel nanowires that is four times the observation in a bulk lattice. In a crystal the elastic strain is limited by the onset of inelastic processes such as dislocation, displacive deformation, twinning and stress-induced phase transformations ... The size of nanocrystals provides a limitation on dislocation activity and associated stress-induced deformation. At a first glance, dislocation-mediated plastic deformation is expected to become inactive below a critical particle size of few nanometers [130]. For example, the critical shear stresses required to nucleate a perfect dislocation varies as 1/R where R is the radius [179] . This explains why inelastic processes are not dominant at nanoscale allowing large mismatches.

## 8. Application to plasmonics

### *8.1. Metal/metal based plasmonic core shell structures*

Optical properties of such core/shell (metal/semiconductor or insulator) nanostructures are based on the interaction of the localized surface plasmon resonance (LSPR) supported by the metal core with the medium of the shell or vice versa. As it is well known, the LSPR is strongly dependent of the surrounding environment. Thus, depending of the nature of the shell, a large range of optical behavior will be possible. Plasmonic spherical nanoshells have been extensively studied. They exhibit a large degree of tenability

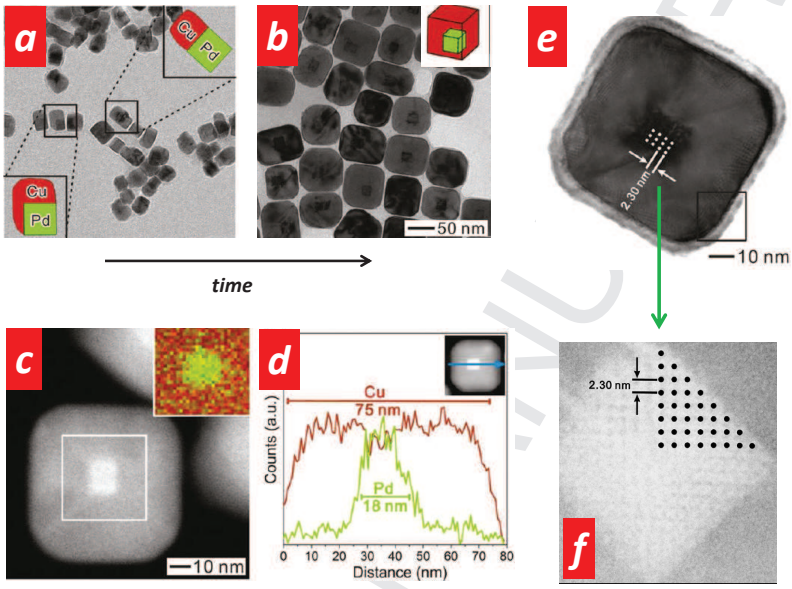


Figure 22: (a) TEM image at the beginning of the growth (20 mn) and (b) after 120 mn. The initial morphology is of Janus type , the final is a core/shell structure. HAADF-STEM image (c) EDX mapping (inset) and (F) line-scan profile indicates that the core is not located at the centre of the core/shell structure. (e) TEM image of a $Pd@Cu$ core/shell nanocube grown from an octahedral seed of Pd and (f) TEM image magnification of the core region shows the Moiré pattern with a spacing D=2.30nm between two bright or dark stripes in agreement with $D = d_1 d_2/(d_2 - d_1) = 2.22nm$, $d_1$ and $d_2$ being the spacing of the two sets of planes involved in the interference calculated from the lattice spacing of {200} planes for both Pd and Cu (lattice constant Pd 0.38824 nm, Cu 0.36077 nm, respectively). (After the original figures from Jin *et al* [177])

that greatly exceeds that of solid metallic nanospheres. The purely metal-based plasmon NPs are widely used to enhance Raman and photoluminescence signal of surrounding systems including quantum dots, molecules and biomolecules [3]. Let us consider the simplest case of a spherical nanoparticle, the polarizability $\alpha$ derived from electrostatics is [180]:

$$\alpha = \frac{(\epsilon_{shell} - \epsilon_m)(\epsilon_{core} + 2\epsilon_{shell}) + \rho(\epsilon_{core} - \epsilon_{shell})(\epsilon_m + 2\epsilon_{shell})}{(\epsilon_{shell} + 2\epsilon_m)(\epsilon_{core} + 2\epsilon_{shell}) + \rho(\epsilon_{core} - \epsilon_{shell})(\epsilon_m + 2\epsilon_{shell})} \tag{7}$$

where R is the outer radius, $\rho = (R/R_{core})^3$ is the core volume fraction and $\epsilon_{core}$, $\epsilon_{shell}$ and $\epsilon_m$ are the core, shell and environment dielectric functions, respectively. If the shell thickness is small compared to the core thickness, ($\rho \to 1$), the polarizability supports a resonance for the well known condition ($\Re[\epsilon]$ the real part)

$$\Re[\epsilon_{core}] = -2\epsilon_m \tag{8}$$

Contrarily, If the core thickness is small compared to the shell thickness, ($\rho \to 0$), the polarizability supports a resonance for the condition

$$\Re[\epsilon_{core}] = -2\Re\epsilon_{shell} \tag{9}$$

For small nanoparticle absorption ($C_{abs}$) and scattering ($C_{scat}$) cross sections are directly derived from the polarizability

$$C_{abs} = k\Im\alpha \tag{10}$$

$$C_{scat} = \frac{k^4}{6\pi}|\alpha|^2 \tag{11}$$

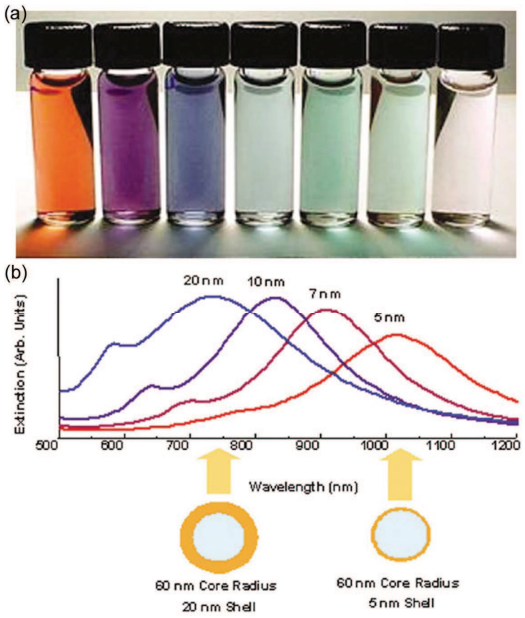


Figure 23: (a) Visual demonstration of the tunability of metal nanoshells. (b) Optical resonances of gold shell-silica core nanoshells as a function of their core/shell ratio. Respective spectra correspond to the NPs depicted beneath. after the original figures from Loo *et al* [181]

Thus, by tuning the core volume fraction and the environment of the core/shell structure, the LSPR and consequently the maximum of absorption and scattering can be tuned under control as shown figure 23 by increasing the thickness of the shell. It has to be noted that the extinction band of core/shell is wider than for metal nanoparticle due to the damping by the outer and the inner nano shell dielectric interface. It implies a drastic reduction of the plasmon lifetime (which is inversely proportional to the width of the extinction band).

*8.2. Metal in dielectric medium*

In this part, we review the case of hybrid NPs combining a noble metal and a semiconducting or an insulator in core and shell, alternatively. The localized surface plasmon resonances (LSPR) accessible through the optical excitation of noble metal NPs (Au, Ag) offer intriguing possibilities in terms of forming hybrid nanostructures. A limiting factor for ultimately down-scaling and integrating devices is the weakening of light-matter coupling at the nanoscale. For this reason, engineering nanostructures with resonantly enhanced light-matter interactions is a very promising approach for emerging fields, including nano-biophotonics and nano-energy. The plasmon-exciton resonant nature enables to address this challenge.

Incorporation of plasmonic NPs is currently investigated to enhance light absorption and photocurrent generation in thin film inorganic solar cells. That could significantly reduce the quantity of material required and hence the cost of thin film photovoltaics. Brown *et al* [182] (fig.24 have incorporated core/shell $Au - SiO_2$ NPs into dye-sensitized solar cells in a compatible way with the state-of-the-art processing and technology. It results in plasmon-enhanced light absorption, photocurrent, and efficiency for solid-state dye-sensitized solar cells. They show by spectroscopic investigation that plasmon-enhanced photocarrier generation competes well with plasmons oscillation damping.

The nature of plasmonic enhancement generally depends on the relative spectral overlap. When the metal surface plasmon frequency is away from the dielectric resonant response, i.e. the off-resonant condition, the improvement is expected with the same spectral dependence as the surface plasmon.

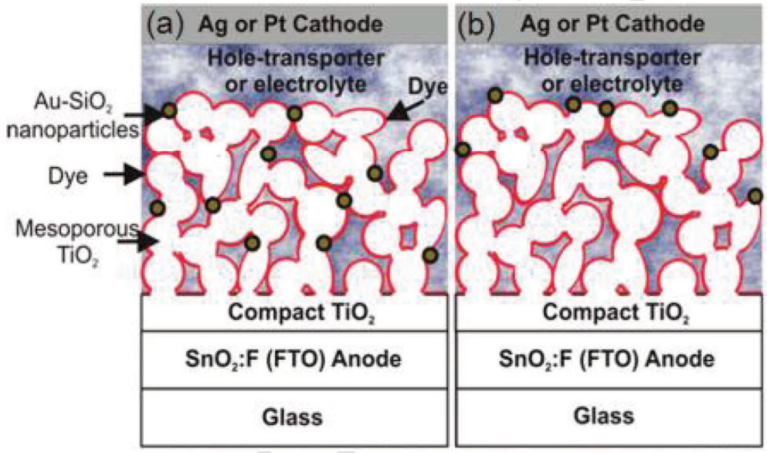


Figure 24: Schematic illustration of the structure of dye-sensitized solar cells ($TiO_2$ NPs are around 20 nm in diameter) incorporating core/shell $Au - SiO_2$ (around 15 nm in diameter) NPs via two approaches (from the reference [182]).

When the resonant condition is achieved, it can lead to novel optical features with stronger enhancement. For example, the control by optical Stark effect (OSE) (see fig. 25) of coherent quantum schemes of spins in semiconductors could promote new physical principles to be used in devices, with the potential for realizing quantum devices based on spin qubits. The optical Stark shift is proportional to the square of the electric field magnitude of subresonant light and to the dipole moment characterizing light-matter interaction, divided by the energy detuning (defined as the difference between resonant bandgap and sub-resonant excitation). The control of both OSE and the spin manipulation has been achieved by tuning plasmon resonance intensity and frequency in Au-CdSe core/shell nanostructures [183]. The demonstration of a sizable OSE has been achieved at substantial energy detuning in a cavity-free colloidal metal-semiconductor core/shell hetero-nanostructure [184]. In that case, the metal surface plasmon is tuned to resonate spectrally with a semiconductor exciton transition. In addition, this resonantly enhanced OSE exhibits polarization dependence, thus providing a viable mechanism for coherent ultrafast spin manipulation within colloidal nanostructures.

Considering that the refractive index of the material surrounding metal NPs plays a major role in wavelength and intensity of the plasmon resonance, another opportunity consists in combining a material that can undergo a strong metal-insulator transition with Au. Such a transition can be provoked by temperature, composition, redox potential, or pressure and it is accompanied with a strong transition in the optical properties. It should result in an active nanomaterial with switchable optical properties. Few compounds, such as $VO_2$ or $WO_3$, exhibit metal-insulator transitions and,

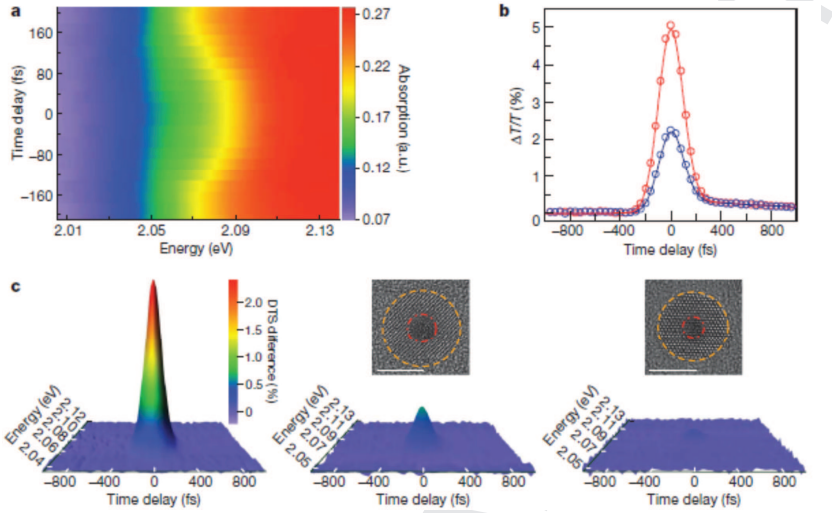


Figure 25: Tunable plasmon-exciton resonantly enhanced OSE and its polarization dependence in Au-CdSe nanostructures. a) Time-resolved linear optical absorption spectra with sub-resonant excitation energy at 1.892 eV. The sub-resonant and probe laser beams are copolarized. The absorption intensity is shown color-coded. b) Polarization dependence of OSE measured by differential transmission spectra (DTS). Red and blue circles are experimental DTS (at a probe energy of 2.077 eV) obtained with respectively co- and counter-polarized sub-resonant excitation at 1.892 eV. c) Temporal and spectral mapping of the DTS difference of co- and counter-polarized sub-resonant excitation and probe, and its dependence on the diameter of the Au core: left, 4.3 nm; middle, 3.3 nm; right, 2.4 nm. For all three samples, the thickness of the monocrystalline CdSe shell remains the same (2.8 nm). The energy detuning DE for data shown left, middle and right are respectively 186, 172 and 106 meV. Insets, high resolution TEM images of samples. Red and orange dashed curves are guides to the eye for the core-boundary and the shell-boundary, respectively. Scale bar, 5 nm (from the reference [184])

hence, transitions in their optical properties. However, a proof-of-concept has not yet been reported, as hybrid NPs $VO_2 - Ag$ or Au have not yet been synthesized.

Not only do these plasmonic nanomaterials strongly interact with light, but their excitation gives rise to near-fields which extend well beyond their physical dimensions. Thus, there exists the strong possibility that these plasmon oscillations will fundamentally alter the properties of nearby nanomaterials. The development of core/shell nanostructures that display metal-enhanced fluorescence (MEF) is a very active field [185, 186, 187, 188]. MEF affects the emission of nearby fluorophores by enhancing excitation and emission rates. For systems exploiting Förster resonant energy transfer (FRET) effects, MEF can improve FRET efficiency and range by increasing the strength of donor-acceptor interactions. It is achieved by placing the donor-acceptor pairs in proximity to metal NPs. The investigation and the exploitation of insulator-coated metal NPs to enhance fluorescence of nearby fluorescent molecules or quantum dots have been reviewed later [189]. Here, we review the case of metal-based NPs which incorporate directly the fluorophore within the core/shell, either by using a semiconducting material, or by doping an insulating material. This can be illustrated by Ag-core/$SiO_2$ spacer/[$SiO_2$ + acceptor]/[$SiO_2$ + donor] systems where the spacer thickness is adjusted to optimize the metal-fluorophores distance and the fluorescence enhancement [190]. Indeed, MEF is most efficient when the metal and the fluorophore are separated by several nanometers in order to avoid quenching by the metal. These core/shell MEF-capable NPs provide several advantages. The interaction with the metallic core greatly enhances excitation efficiency

and emissive rates, while the reduction of self-quenching due to the silica spacer makes possible the incorporation of larger amounts of dye molecules. Additionally, the shell protects the organic dyes against irreversible photodegradation. Such features are particularly suited for biosensing applications or for cell imaging work. Similarly, core/shell $Ag@SiO_2$@mesoporous $SiO_2$ nanocarriers were synthesized to optimize the separating distance between the metal and the fluorophores (eosin isothiocyanate) incorporated into the mesoporous $SiO_2$ shell [96].

As well known, plasmonic nanostructures are used to increase low scattering cross section processes as Raman or fluorescence. As described by Gaponenko [180], the intensity of such a process can be written as

$$I(\omega') = I_l(\omega)[interactionterm]D(\omega') \tag{12}$$

with $I(\omega')$ the outcoming radiation intensity, $I_l(\omega)$ the incoming radiation intensity and $D(\omega')$ the density of states at the final frequency. Considering this general formula for Raman or fluorescence amplification by plasmon, the outcoming radiation corresponds to the local field enhancement. Thus, core/shell NPs are good candidate to improve the scattered signal because of (i) the tunability of the plasmon resonance with the thickness of the shell, (ii) the possibility to tune under control the distance between the metal and the nanoobject (molecule, quantum dots etc.) [191] and (iii) avoid the aggregation [192].

Moreover, metal NPs are lossy systems due to the strong absorption of light. In order to compensate those losses, the dielectric shell (or core) can be doped by fluorescent emitters or semiconducting QDs (i.e. a gain medium).

The emission energy is coupled from the excited state of the gain media to the plasmon state by near field interactions. As a definition, a plasmophore is a core/shell system composed of metal and gain medium. The dielectric function of such gain medium can be expressed as [193]

$$\epsilon_{gain} = (n^2 - k^2) + 2ink \tag{13}$$

with n the real part of the refractive index, and k the gain coefficient. Thus, the extinction ($C_{ext}$), scattering ($C_{scat}$) and absorption ($C_{abs}$) cross sections can be determined as a function of the gain coefficient (see figure Figure 26).

Unfortunately, this simple approach is not suitable to describe the behavior of such a system when the losses are completely compensated (i.e. $C_{ext} = 0$). Bergman and Stockman [196, 197] have proposed a theory allowing to describe the behavior in case of complete compensation of the losses. In such case, a phenomenon, called SPASER for Surface Plasmon Amplification by Stimulated Emission of Radiation will occur [198, 199]. The SPASER is a localized source of energy induced by the stimulated emission of surface plasmon. This is not necessarily a radiative nano source (i.e. a demonstration nanolaser). The Noginov's group has made an experimental demonstration of such a SPASER in the radiative case as shown figure Figure 27 [195].

*8.3. Magneto-plasmonic core/shells*

In most cases iron oxide NPs coated with gold or iron shells retain their ferri- or antiferro-magnetic properties [157, 158]. Very small superparamagnetic iron oxide NPs (SPION) coated with a gold shell displayed a slight shift

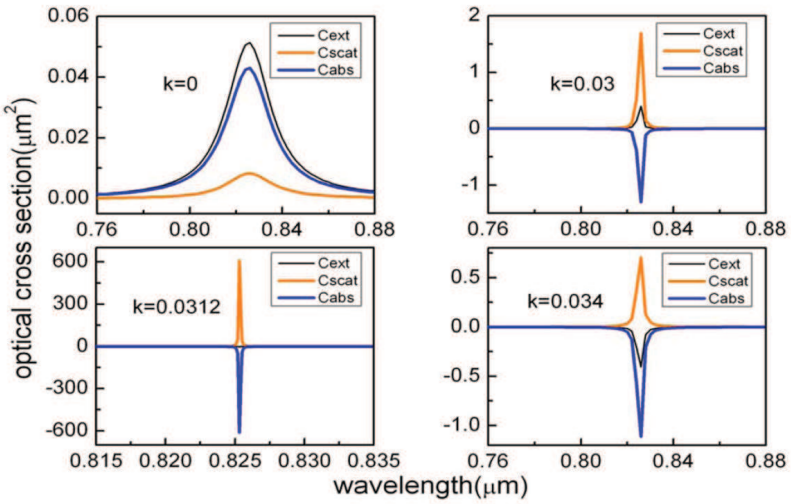


Figure 26: (a) Calculated optical cross-section spectra for a core/shell (metal/gain medium) nano system with different gain coefficients (k) as noted. after the original figures from Liu *et al* [194]. (b) Normalized extinction (1), excitation (2), spontaneous emission (3), and stimulated emission (4) spectra of Au/silica/ dye NPs. (Insert) Diagram of the hybrid nanoparticle architecture indicating dye molecules throughout the silica shell. From Noginov *et al.* [195].

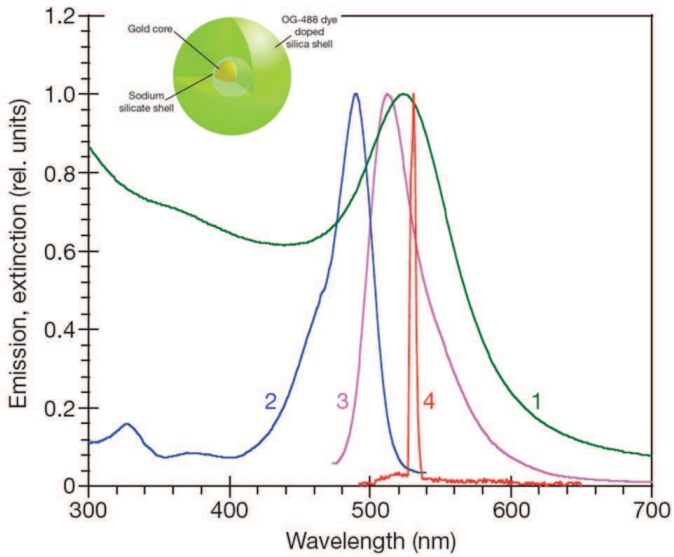


Figure 27: Normalized extinction (1), excitation (2), spontaneous emission (3), and stimulated emission (4) spectra of Au/silica/ dye NPs. (Insert) Diagram of the hybrid nanoparticle architecture indicating dye molecules throughout the silica shell. From Noginov *et al.* [11]

(decrease) of the blocking temperature and a decrease in their susceptibility in comparison to the uncoated NPs, which is believed to reflect the less efficient coupling of the magnetic cores as a result of interparticle spacing [78, 200, 201, 157]

In contrast, the plasmonic properties of the metallic shell are strongly influenced by the high dielectric constant of the magnetic cores. Indeed, gold shells grown on magnetite exhibit a surface plasmon resonance at larger wavelengths compared to shells of similar size grown over silica. In addition, this resonance is further red-shifted with increasing shell thickness, in contrast to the blue shift observed for shells grown over silica [78, 201, 202]. This lower energy resonance of the plasmon is related to the permittivity of the core (high for Fe oxide and low for silica) and its variation with increasing the size of the shell results from the decrease of the coupling between the shell plasmons associated with the outer and the inner side of the gold shell (figure 28). Note that the direction of the plasmon shift can be controlled by growing either Au or Ag on a $Fe_3O_4$@$Au$ nanoparticle.

The transfer of spin-polarization from iron oxide into gold was evidenced in Au@Fe-oxide NPs, which constitutes the unique report of an induced magnetic moment transferred from a transition-metal oxide into a non-magnetic metal [204]. Synergetic effects from the combination of gold with oxide materials were also reported in the field of catalysis, but are still a matter of debate. Catalysis experiments have suggested that core/shell nanostructures present more pronounced synergetic effect than other heterostructures made from the same materials. Catalytic core/shell NPs are mostly metal@oxide such as $Au$@$Fe_2O_3$ [205], $Au$@$SnO_2$ [206] but oxide@metal systems are also

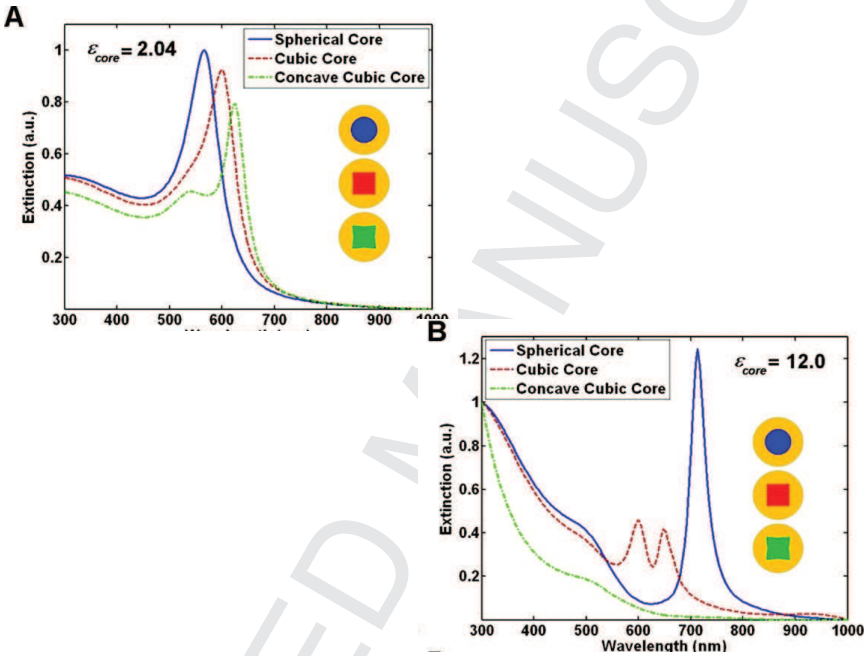


Figure 28: Theoretical comparison of extinction spectra for gold nanoshells with cores dielectrics corresponding to (A) silica ($\epsilon = 2.04$) and (B) an artificial material with $\epsilon ==$ 12.0, for different shapes. The outer radius of the shell is $r_2 = 50$ nm, and the effective radius of the core is $r_{eff} = 32$ nm. from reference [203]

studied (*eg* $Fe_3O_4$ coated with a thin layer ( 0.5 nm) of gold [159]).

*8.4. Metal/semiconductor core/shell NPs: anisotropy*

Besides spherical nanostructures, anisotropic systems such as core/shell nanorods, formed through the encapsulation of a semiconductor with a noble metal nanoshell, provide a straightforward geometry for studying the hybrid response. With the capability to tune the resonant plasmon frequency through alterations to nanoshell shape, thickness, overall radius, and dielectric environment firmly established, it follows that the degree of coupling in a core/shell nanorod should also become highly tunable. Polarization effects of emission in nanorods has been demonstrated in Au nanorod cores and oxazine 725-embedded mesostructured silica shells [207]. It is reported that the degree of polarization is equal to that of the light scattered by the nanorod and varying from 0 to 1 as the longitudinal plasmon resonance wavelength is increased. Further analysis indicates that the interactions of the plasmon resonance of the nanorod with the excitation and emission processes of the fluorophores are temporally separated under unsaturated excitation conditions. The emission polarization is found through electrodynamic calculations to arise from the plasmon-coupled emission instead of the plasmon-enhanced excitation polarization. The emission carries the direction and polarization properties that are essentially determined by the dipolar plasmon of the nanorod antenna. It provides concrete evidence for the plasmophore that has been proposed for plasmon-enhanced fluorescence [208]. Exciton-plasmon interactions have also been reported in Au-CdS nanorods, with heterostructures synthesized from seeds of gold-nanorods and $Ag_2S$ employed as an interim layer that favors CdS shell formation through a cation-exchange

process [209]. A red-shift of the longitudinal surface plasmon resonance was evidenced, that can be tailored by the shell thickness while the photoluminescence of CdS is quenched under UV light excitation. In addition, an enhanced and plasmon-governed two-photon luminescence under near-infrared pulsed laser excitation is observed.

The relaxation processes between excitons and plasmons were also examined in vertically aligned CdTe-Au core/shell nanorods [210]. Here, the core/shell nanorods were fabricated by using a vapor-liquid-solid (VLS) growth mode on a substrate and the gold shell was subsequently sputtered onto the nanorods. The dependence of the plasmon field enhancement for two thicknesses of the gold shell (15 and 26 nm) was determined by angular-dependent pump (at 400 nm pulses)-probe measurements. The temporal relaxation of the excited carriers was measured with a 770 nm probe beam, which coincides with the band gap edge of CdTe. The analysis of possible electronic relaxation enhancement mechanisms and the simulation of discrete dipole approximation (DDA) properties drive to the conclusion that by increasing the metallic nanoshell thickness, the relaxation processes change from multiple enhancement mechanisms, dominated by highly anisotropic Auger processes, to a mechanism involving first-order excited electron ejection process. The former is shown to give rise to nonexponential anisotropic decays in the dipolar plasmon field of the thin nanoshell, while the latter exhibits an exponential isotropic decay in the unpolarized plasmonic field of the thick nanoshell.

Besides the increasing interest for linear optical processes, plasmonic NPs can also be used to enhance non-linear optical NLO effects, with an increas-

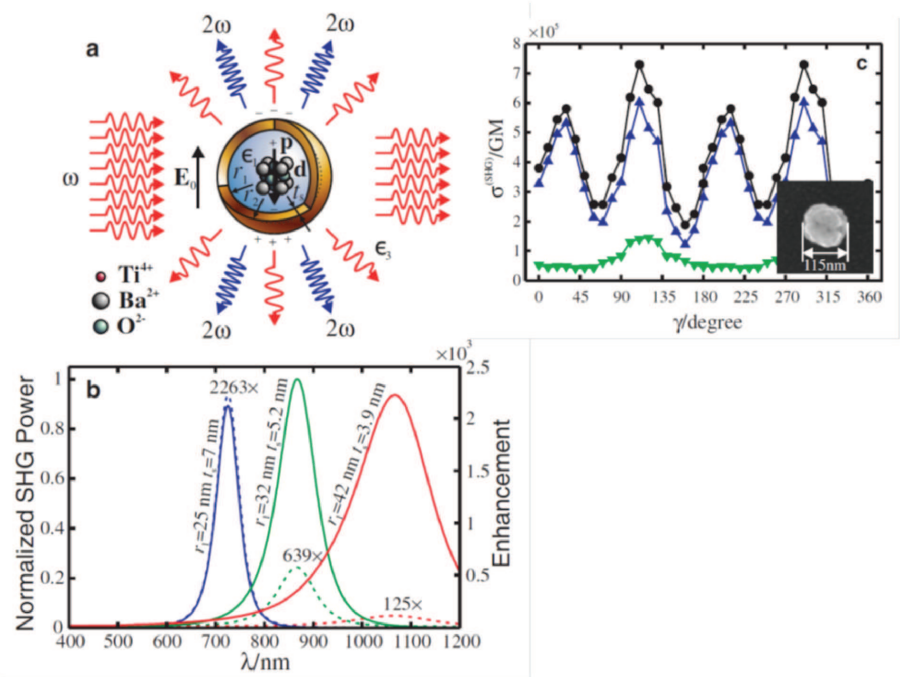


Figure 29: Enhancement and tunability of plasmonic SHG nanocavities. (a) Scheme of $BaTiO_3$@$Au$ SHG nanocavities. (b) Calculation with various structural parameters. Solid curves represent radiation power in second-harmonic frequency normalized to the maximum radiation power among the three examples. Dotted curves represent the factor of SHG enhancement compared to the core. (c) Measured SHG scattering cross section of the $BaTiO_3$@$Au$ core/shell nanocavity shown in the insets. Blue up triangles and green

ing demand for subwavelength coherent light sources. While second-harmonic generation (SHG) is prohibited in bulk centrosymmetric materials, nano scale SHG can be achieved by breaking the symmetry through interfaces, imperfect spheres, and asymmetric shapes. However, NLO harmonic generation is generally inefficient at such a small scale. This problem has been recently addressed by the incorporation of $BaTiO_3$ as a noncentrosymmetric medium into a plasmonic gold shell [211] (fig. 29). It has been shown that such nanocavities act as subwavelength coherent light source through second-harmonic generation, with a 500 times enhancement than in the second-harmonic radiation power. An expected enhancement of over 3500 times has been estimated through calculation.

## 9. Conclusion

The core/shell structures are a good example of the segregation effect inside an alloy at nanoscale. At the beginning, the shell was dedicated to the *invasive* protection of the core. Going forward, "smart shells" were introduced with a compromise between a good chemical or mechanical protection and the transparency towards a selected property. Nowadays, the core/shell structures are new systems where the enhancement of a given property is expected with respect to the native components. This was first evidenced in semiconductors and now extended to metal-metal and mixed systems. This enhancement is more or less understood in the light of the "interface" effect between the core and shell. A major breakthrough will be in the future to monitor and to understand the role of the interface. This is the key point for the development of tailored materials based from core/shell NPs opening

the way to bifunctional nanoparticles.

## 10. Acknowledgement

This review is proposed by the the members of the "nanoconstruction work group" belonging to the OMNT (Observatoire des micro et nanotechnologies) French agency CNRS CEA Unité Mixte de Service CNRS-CEA $n^o$ 2920 (http://www.omnt.fr/index.php/en/). Peter Reiss P.R. thanks the French National Research Agency (grant number ANR-12-NANO-0007, NANOFRET) for financial support.

## References

[1] B.E.Cohen, Nature 467 (2010) 407–408.

[2] A. S. Kirakosyan, T. V. Shahbazyan, The J. of Chem. Phys. 129 (2008) 034708 1–7.

[3] M. Cortie, A. M. McDonagh, Chem. Rev. 111 (2011) 3713–3735.

[4] A. M. Smith, A. M. Mohs, S. Nie, Nature Nanotechnology 4 (2009) 56–63.

[5] H. Kim, M. Achermann, L. P. Balet, J. A. Hollingsworth, V. I. Klimov, J. Am. Chem. Soc. 127 (2005) 544–546.

[6] S. Sun, W. Wang, L. Zhang, M. Shang, L. Wang, Catalysis Comm 11 (2009) 290–293.

[7] D. M. Fouad, M. B. Mohamed, Nanotechnology 22 (2011) 455705 1–8.

[8] J. Tang, K. Kemp, S. Hoogland, K. S. Jeong, H. Liu, L. Levina, M. Furukawa, X.Wang, R. Debnath, D. Cha, K. Chou, A. Fischer, A. Amassian, J. B. Asbury, E. H. Sargent, Nature materials 10 (2011) 765–771.

[9] R. G. Chaudhuri, S. Paria, Chem. Rev. 112 (2012) 2373–2433.

[10] J.Garcia-Torres, E. Vallés, E. Goméz, J Nanopart Res 12 (2010) 2189–2199.

[11] S.-H. Lee, C.-W. Yi, K. Kim, J. Phys. Chem. C 115 (2011) 2572–2577.

[12] V.Radmilovic, C.Ophus, E. Marquis, M.D.Rossell, A.Tolley, A.Gautam, M.Asta, U.Dahmen, J. Phys. Chem. C 10 (2011) 710 1–5.

[13] J. Qi, J. Chen, G. Li, S. Li, Y. Gao, Z. Tang, Energy Environ. Sci. 5 (2012) 8937–8941.

[14] P. Reiss, M. Protiere, L. Li, Small 5 (2009) 154–168.

[15] S. Santra, R.Tapec, N. Theodoropoulou, J. Dobson, A. Hebard, W.Tan, Langmuir 17 (2001) 2900–2906.

[16] S. Chang, L. Liu, S. Asher, J. Am. Chem. Soc. 116 (1994) 6739–6744.

[17] P. Tartaj, T. Gonzalez-Carreno, C. Serna, Adv. Mater. 13 (2001) 1620–1624.

[18] P. Tartaj, T. Gonzalez-Carreno, C. Serna, Adv. Mater. 16 (2004) 529–533.

[19] R. G. Chaudhuri, S. Paria, Chem. Rev. 112 (2012) 2373.

[20] L. Wang, X. Wang, J.Luo, B. Wanjala, C. Wang, N. Chernova, M. Engelhard, Y. Liu, I. Bae, C. Zhong, J. Am. Chem. Soc. 132 (2010) 17686–17689.

[21] W. Baaziz, B. P. Pichon, C. Lefevre, C. Ulhaq-Bouillet, J.-M. Greneche, M. Toumi, T. Mhiri, S. Bégin-Colin, J. Phys. Chem C 117 (2013) 11436–11443.

[22] V. Srdi, B. Moji, M. Nikoli, S. Ognjanovi, Processing and Application of Ceramics 7 (2013) 45–62.

[23] L. Lee, R. M. Anisur, K. W. Kim, W. S. Kim, T.-J. Park, E. J. Kang, I. S. Lee, Chem. Mater. 24 (2012) 682–687.

[24] J.H.Lee, J.T.Jang, J.S.Choi, S. Moon, S. Noh, J. Kim, J. Kim, I. Kim, K. Park, J. Cheon, Nature Nano. 6 (2011) 418–422.

[25] I. Robinson, L. D. Tung, S. Maenosono, C. Waltid, N. T. K. Thanh, Nanoscale 2 (2010) 2624–2630.

[26] J. J. Li, Y. A. Wang, W. Z. Guo, J. C. Keay, T. D. Mishima, M. B. Johnson, X. G. Peng, J. Am. Chem. Soc. 125 (2003) 12567–12575.

[27] B. Mahler, P. Spinicelli, S. Buil, X. Quelin, J.-P. Hermier, B. Dubertret, Nature Materials 7 (2008) 659–664.

[28] F. Silva, M. Carvalho, R. Mendona, W. A. Macedo, K. Balzuweit, P. Reiss, M. A. Schiavon, Nanoscale Research Letters 7 (2012) 536 1–10.

[29] A.L.Rogach, T.Franzl, T. A. Klar, J.Feldmann, N.Gaponik, V. Lesnyak, A. A. Eychmüller, Y. Rakovich, J. F. Donegan, J. of Phys. Chem. C 111 (2007) 14628–14637.

[30] A. Shavel, N. Gaponik, A. Eychmüller, J. of Phys. Chem. B 108 (2004) 5905–5908.

[31] L. Li, P. Reiss, J. Am. Chem. Soc. 130 (2008) 11588–11589.

[32] W. Bae, H.Hur, S. Lee, J. Am. Chem. Soc. 20 (2008) 531–539.

[33] W. R. Lee, M. G. Kim, J. R. Choi, J. I. Park, S. J. Ko, S. J. Oh, J. Cheon, J. Am. Chem. Soc. 127 (2005) 16090–16097.

[34] J. Rivest, P. Jain, Chem. Soc. Rev. 42 (2013) 89–96.

[35] J. M. Pietryga, D. J. Werder, D. J. Williams, J. L. C. R. D. Schaller, V. Klimov, J. A. Hollingsworth, J. Am. Chem. Soc. 130 (2008) 4879–4885.

[36] R. B. H. Li, R. Krahne, G. Bertoni, M. Alcocer, C. D'Andrea, F. Scotognella, F. Tassone, M. Zanella, M. D. Giorgi, L. Manna, ACS Nano 6 (2012) 1637–1647.

[37] L. J. Lauhon, M. S. Gudiksen, D. Wang, C. M. Lieber, Nature 420 (2002) 57–61.

[38] R. Anton, Carbon 46 (2008) 656–662.

[39] Y. Cohin, O. Mauguin, L. Largeau, G. Patriarche, F. Glas, E. Sondergard, J.-C. Harmand, Nano Letters 13 (2013) 2743–2747.

[40] S. Habas, H. Lee, V. Radmilovic, G. A. Somorjai, P. Yang, Nature Materials 6 (2007) 692–697.

[41] G. Gadd, M. Collela, M. Blackford, A. Dixon, P. Evans, D. McCulloch, S. Bulcock, D. Cockayne, Carbon 39 (2001) 1769–1787.

[42] J. C. Love, B. D. Gates, D. B. Wolfe, K. E. Paul, G. M. Whitesides, Nano Letters 2 (2002) 891–894.

[43] Y. Lu, H. Xiong, X. Jiang, Y. Xia, M. Prentiss, G. M. Whitesides, Journal of the American Chemical Society 125 (2003) 12724–12725.

[44] C. M. Sweeney, W. Hasan, C. L. Nehl, T. W. Odom, The J. of Phys. Chem. A 113 (2009) 4265–4268.

[45] S. Rusponi, T. Cren, N. Weiss, M. Epple, P. Buluschek, L. Claude, H. Brune, Nature Materials 2 (2003) 546–551.

[46] R. J. Davies, M. Bowker, P. R. Davies, D. J. Morgan, Nanoscale (2013) 9018–9022.

[47] M. Lewandowski, Y. Sun, Z.-H. Qin, S. Shaikhutdinov, H.-J. Freund, Applied Catalysis A: General 391 (2011) 407–410.

[48] F. Silly, M. R. Castell, The J. of Phys. Chem. B 109 (2005) 12316–12319.

[49] O.Waser, R. Büchel, A.Hintennach, P. N. ak, S.Pratsinis, Journal of Aerosol Science 42 (2011) 657–667.

[50] A. Quinsac, Y. Leconte, C. Reynaud, N. H. Boime, Patent (2012) FR 1261243.

[51] P. Melinon, P. Keghelian, A. Perez, C. Ray, J. Lerme, M. Pellarin, M.Broyer, M.Boudeulle, B. Champagnon, J.L.Rousset, Phys. Rev. B 58 (1998) 16481–16490.

[52] A.Perez, P.Melinon, V.Dupuis, L.Bardotti, B.Masenelli, F.Tournus, B.Prevel, J.Tuaillon-Combes, E.Bernstein, A.Tamion, N.Blanc, D.Tainoff, O.Boisron, G.Guiraud, M.Broyer, M.Pellarin, N. Fatti, F.Vallee, E.Cottancin, J.Lerme, J.L.Vialle, C.Bonnet, P.Maioli, A.Crut, C.Clavier, J.L.Rousset, F.Morfin, Int. J. of Nanotechnology 7 (2010) 523–574.

[53] M.Gaudry, E.Cottancin, M.Pellarin, J.Lerme, L.Arnaud, J. Huntzinger, J.L.Vialle, M.Broyer, J. Rousset, M. Treilleux, P.Mélinon, Phys. Rev. B 67 (2003) 155409 1–10.

[54] K. Hoshino, T. Naganuma, Y. Yamada, K. Watanabe, A.Nakajima, K. Kaya, Chemistry-a European Journal 97 (1992) 3803–3807.

[55] W. Bouwen, P. Thoen, F. Vanhoutte, S. Bouckaert, F. Despa, H. Weidele, R. Silverans, P. Lievens, Rev. Sci. Instrum. 71 (2000) 54 1–5.

[56] Y. Jo, S.-B. Wen, J. Phys. D: Appl. Phys. 44 (2011) 305301 1–11.

[57] K. Urban, Science 321 (2008) 506–510.

[58] D. Ferrer, D. Blom, L. Allard, S. Mejía, E. Pérez-Tijerina, M. José-Yacamán, J. of Mat. Chem. 18 (2008) 2442–2446.

[59] L. Gan, R. Yu, J. Luo, Z. Cheng, J. Zhu, The J. of Phys. Chem. Lett. 3 (2012) 934–938.

[60] P. Schattschneider, I. Ennen, S. Löffler, M. Stöger-Pollach, J. Verbeeck, Journal of Appl. Phys. 107 (2010) 09D311–1–09D311–6.

[61] N. Zaluzec, Microscopy Today 17 (2009) 56–59.

[62] M. Cabié, S. Giorgio, C. Henry, M. Axet, K. Philippot, B. Chaudret, The J. of Phys. Chem. C 114 (2010) 2160–2163.

[63] J. Evans, K. Jungjohann, N. Browning, I. Arslan, Nano lett. 11 (2011) 2809–2813.

[64] E. Snoeck, C. Gatel, L. Lacroix, T. Blon, S. Lachaize, J. Carrey, M. Respaud, B. Chaudret, Nano Letters 8 (2008) 4293–4298.

[65] Y.-H. Xu, J.-P. Wang, Adv. Mater. 20 (2008) 994–999.

[66] F. Tournus, K. Sato, T. Epicier, T. J. Konno, V. Dupuis, Phys. Rev. Lett. 110 (2013) 055501 1–5.

[67] A. J. L. Rousset, A. Cadrot, Phys. Rev. B 58 (1998) 2150–2156.

[68] R. Leary, P. Midgley, J. Thomas, Accounts of Chemical Research 45 (2012) 1782–1791.

[69] P. Midgley, R. Dunin-Borkowski, Nature Materials 8 (2009) 271–280.

[70] S. V. Aert, K. Batenburg, M. Rossell, R. Erni, G. V. Tendeloo, Nature 470 (2011) 374–377.

[71] Z. Saghi, D. Holland, R. Leary, A. Falqui, G. Bertoni, A. Sederman, L. Gladden, P. Midgley, Nano Letters 11 (2011) 4666–4673.

[72] S. Kuchibhatla, V. Shutthanandan, T. Prosa, P. Adusumilli, B. Arey, A. Buxbaum, Y. Wang, T. Tessner, R. Ulfig, C. Wang, S. Thevuthasan, Nanotechnology 23 (2012) 215704 1–5.

[73] Q. Song, Z. J. Zhang, J. Am. Chem. Soc. 134 (2012) 10182–10190.

[74] Y. Zhao, P. Chen, B. Zhang, D. Su, S. Zhang, L. Tian, J. Lu, Z. Li, X. Cao, B. Wang, M. Wei, D. Evans, X. Duan, Chemistry-a European Journal 18 (2012) 11949–11958.

[75] K. Huang, R. Demadrille, M. G. Silly, F. Sirotti, P. Reiss, O. Renault, ACS nano 4 (2010) 4799–4805.

[76] B. N.Wanjala, R. L. J. Luo, B. Fang, D. Mott, P. Njoki, M. Engelhard, H. R. Naslund, J. K. Wu, L. Wang, O. Malis, C.-J. Zhong, Chem. Mater. 22 (2010) 4282–4294.

[77] K.-J. Jeon, H. R. Moon, A. M. Ruminski, B. Jiang, C. Kisielowski, R. Bardhan, J. J. Urban, Nature Materials 10 (2011) 286–290.

[78] L. Wang, J. Luo, Q.Fan, M.Suzuki, I. Suzuki, M. Engelhard, Y.Lin, N. Kim, J. Wang, C. Zhong, The J. of Phys. Chem. B 109 (2005) 215933–21601.

[79] H. Park, M. Schadt, L. Wang, I. Lim, P. Njoki, S. Kim, M. Jang, J. Luo, C. Zhong, Langmuir 23 (2007) 9050–9056.

[80] V. Salgueiriño-Maceira, M. Correa-Duarte, M. Farle, A. Lopez-Quintela, K. Sieradzki, R. Diaz, Chemistry of Materials 18 (2006) 2701–2706.

[81] X.Ji, R. Shao, A. Elliott, R. Stafford, E. Esparza-Coss, G. Liang, Z. Luo, K. Park, J. Markert, C.Li, The J. of Phys. Chem. C 111 (2007) 6245–6251.

[82] P.Ray, Z.Fan, D. Senapati, A.Singh, Molecular Pharmaceutics 10 (2013) 857–866.

[83] Z. Fan, M. Shelton, A. Singh, D. Senapati, S. Khan, P. Ray, ACS nano 6 (2012) 1065–1073.

[84] U. Tamer, Y. Gündogdu, I. Boyaci, K. Pekmez, Journal of Nanoparticle Research 12 (2010) 1187–1196.

[85] Y. Yin, R. M. Rioux, C. K. Erdonmez, S. Hughes, G. A. Somorjai, A. P. Alivisatos, Science 304 (2004) 711–714.

[86] S. Gullapalli, J. M. Grider, H. G. Bagaria, K.-S. Lee, M. Cho, V. L. Colvin, G. E. Jabbour, M. S. Wong, Nanotechnology 23 (2012) 495605–495615.

[87] Q.Cui, Y.Sha, J.Chen, Z.Gu, J. Nanopart. Res. 13 (2012) 4785–4794.

[88] J. Railsback, A.C.Johnston-Peck, J. Wang, J.B.Tracy, ACS Nano 4 (2010) 1913–1920.

[89] F. Caruso, R. Caruso, H. Mohwald, Science 282 (1998) 1111–1–4.

[90] Y. Xia, Z. Tang, Adv. Funct. Mater. 22 (2012) 2585–2593.

[91] L. Zhang, D. A. Blom, H. Wang, Adv. Funct. Mater. 23 (2011) 4587–4598.

[92] D.-H. Ha, L. Moreau, C. Bealing, H. Zhang, R. Hennig, R. Robinson, J. Mater. Chem. 21 (2011) 11498–11510.

[93] J.Turkevich, G.Kim, Science 169 (1970) 873–879.

[94] R.C.Sekol, X.Li, P.Cohen, G.Doubek, M.Carmo, A.D.Taylor, Applied Catalysis B: Environmental 138-139 (2013) 285–293.

[95] D. Astruc, F. Lu, J. R. Aranzaes, Angew.Chem.Int.Ed. 44 (2005) 7852–7872.

[96] H.Yang, Angew. Chem. Int. Ed. 50 (2011) 2674–2676.

[97] S.J.Hwang, S.J.Yoo, J.Shin, Y-H.Cho, J.H.Jang, E.Cho, Y-E.Sung, S.W.Nam, T-H.Lim, S-C.Lee, S-K.Kim, Scientific Reports 3 (2013) 1309 1–7.

[98] T. Atabaev, H.-K. Kim, Y.-H. Hwang, Nano. Res. Lett. 8 (2013) 357 1–6.

[99] G.Chen, S.Desinan, R.Nechache, R.Rosei, F.Rosei, D.Ma, Chem. Commun. 47 (2011) 6308–6310.

[100] Zhon.Chen, Z. Chen, Patent 100354 (2012) PCT/CA2012/050050.

[101] K. Azawu, M. Fujimaki, C. Rockstuhl, J. Tominanga, H. Murakami, Y. Ohki, N. Yoshida, T. Watanabe, Phys. Chem. Chem. Phys. 130 (2008) 1676–1680.

[102] B. Cheng, Y. Le, J. Yu, J. Hazmat 177 (2010) 971–977.

[103] P. Wang, B. Huang, Y. Dai, M. Whangbo, Phys. Chem. Chem. Phys. 14 (2012) 9813–9825.

[104] Y.-K. Sun, S.-T.Myung, B.-C. Park, J. Prakash, I. Belharouak, K. Amine, Nature Materials 8 (2009) 320–324.

[105] N. Zhang, S. Liu, X. Fu, Y. Xu, J. Phys. Chem. C 115 (2011) 9136–9145.

[106] S. Kim, B. Fisher, H. J. Eisler, M. Bawendi, J. Am. Chem. Soc. 125 (2003) 11466–11467.

[107] L. P. Balet, S. A. Ivanov, A. Piryatinski, M. Achermann, V. I. Klimov, Nano Lett. 17 (2004) 4038–4042.

[108] P. T. K. Chin, C. D. M. Donega, S. S. Bavel, S. C. J. Meskers, N. Sommerdijk, R. A. J. Janssen, J. Am. Chem. Soc. 129 (2007) 14880–14886.

[109] X. H. Zhong, R. G. Xie, Y. Zhang, T. Basche, W. Knoll, Chem. Mater. 4 (2005) 1485–1488.

[110] Y. Chen, J. Vela, H. Htoon, J. L. Casson, D. J. Werder, D. A. Bussian, V. I. Klimov, J. A. Hollingsworth, J. Am. Chem. Soc. 130 (2008) 5026–5027.

[111] P. Reiss, S. Carayon, J. Bleuse, A.Pron, Synth. Met. 139 (2003) 649–652.

[112] D. V. Talapin, I. Mekis, S. Gotzinger, A. Kornowski, O. Benson, H. Weller, J. Phys. Chem. B 108 (2004) 18826–18831.

[113] S. Jun, E. Jang, Angew. Chem. Int. Ed. 52 (2013) 679–682.

[114] H. W. A. Eychmüller, A. Mews, Chem. Phys. Lett. 208 (1993) 59–62.

[115] D. Battaglia, B. Blackman, X. G. Peng, J. Am. Chem. Soc. 127 (2005) 10889–10897.

[116] D. Talapin, R. Koeppe, S. Gotzinger, A. Kornowski, J. Lupton, A. Rogach, O. Benson, J. Feldmann, H. Weller, Nano Lett. 3 (2003) 1677–1681.

[117] D. Talapin, J. Nelson, E. Shevchenko, S. Aloni, B. Sadtler, A. Alivisatos, Nano Lett. 7 (2007) 2951–2959.

[118] L. Carbone, C. Nobile, M. D. Giorg, F. Sala, G. Morello, P. Pompa, M. Hytch, E. Snoeck, A. Fiore, I. Franchini, M. Nadasan, A. Silvestre, L. Chiodo, S. Kudera, R. Cingolani, R. Krahne, L. Manna, Nano Lett. 7 (2007) 2942–2950.

[119] C. Grivas, C. Li, P. Andreakou, P. Wang, M. Ding, G. Brambilla, L. Manna, P. Lagoudakis, Nat Commun. 4 (2013) 2376 1–9.

[120] F. Garcia-Santamaria, S. Brovelli, R. Viswanatha, J. Hollingsworth, H. Htoon, S. Crooker, V. Klimov, Nano Lett. 11 (2011) 687–693.

[121] A. Vaneski, J. Schneider, A. Susha, A. Rogach, APL Materials 2 (2014) 012104 1–6.

[122] S. Deka, K. Miszta, D. Dorfs, A. Genovese, G. Bertoni, L. Manna, Nano Lett. 10 (2010) 3770–3776.

[123] E. Cassette, B. Mahler, J.-M. Guigner, G. Patriarche, B. Dubertret, T. Pons, ACS Nano 6 (2012) 6741–6750.

[124] K. Acharya, R. Khnayzer, T. O'Connor, G. Diederich, M. Kirsanova, A. Klinkova, D. Roth, E. Kinder, M. Imboden, M. Zamkov, Nano Lett. 11 (2011) 2919–2926.

[125] M. Yu, C. S. Jayanthi, S. Y. Wu, Nanotechnology 23 (2012) 235705 1–9.

[126] P.Melinon, B.Masenelli, F.Tournus, A.Perez, Nature Materials 7 (2007) 479–490.

[127] A. S. Barnard, S. P. Russo, I. K. Snook, Phys.Rev B 12 (2003) 073406 1–4.

[128] F. Wang, R. Deng, J. Wang, Q. Wang, Y. Han, H. Zhu, X. Chen, X. Liu, Nature Materials 10 (2011) 968–973.

[129] N. M. Idris, M. K. Gnanasammandhan, J. Zhang, P. C. Ho, R. Mahendran, Y. Zhang, Nature Medecine 18 (2012) 1580–U190.

[130] B.Chen, K.Lutker, S. Raju, J.Yan, W.Kanitpanyacharoen, J.Lei, S.Yang, H.-R. Wenk, H. k. Mao, Q.Williams, Science 338 (2012) 1448–1451.

[131] X.-F. Qiao, J.-C. Zhou, J.-W. Xiao, Y.-F. Wang, L.-D. Sun, C.-H. Yan, Nanoscale 4 (2012) 4611–4623.

[132] Y. I. Park, H. M. Kim, J. H. Kim, K. C. Moon, B. Yoo, K. T. Lee, N. Lee, Y. Choi, W. Park, D. Ling, K. Na, W. K. Moon, S. H. Choi, H. S. Park, S.-Y. Yoon, Y. D. Suh, S. H. Lee, T. Hyeon, Adv. Mat. 24 (2012) 5755–5761.

[133] S. K. W. MacDougall, A. Ivaturi, J. Marques-Hueso, K. W. Kraemer, B. S. Richards, Optics Express 20 (2012) A879–A887.

[134] T. T. Thuy, D. Mott, N. T. K. Thanh, S. Maenosono, RSC Adv. 1 (2011) 100–108.

[135] W. R. Siah, A. LaGrow, M. J. Banholzer, R. D. Tilley, Cryst. Growth Des. 13 (2013) 2486–2492.

[136] F. Grasset, F. Dorson, Y. Molard, S. Cordier, V. Demange, C. Perrin, V. Marchi-Artzner, H. Haneda, Chem. Commun. 39 (2008) 4729–4731.

[137] J. Y. Lilin Zhou, Y. Wei, J. Mater. Chem. 21 (2011) 2823–2840.

[138] J. K. Lai, M. Lai, S. Jandhyam, V. Dukhande, A. Bhushan, C. Daniels, S. Leung, Int J Nanomedicine 3(4) (2008) 533–545.

[139] S. Selvan, P. Patra, C. Ang, J. Ying, Angew. Chem. Int. Ed. 119 (2007) 2448–2452.

[140] D. Yi, S. Selvan, S. Lee, G. Papaefthymiou, D. Kundaliya, J. Ying, J. Am. Chem. Soc. 127 (2005) 4990–4991.

[141] B.Julian-Lopez, C. Boissire, C.Chaneac, D.Grosso, S. Vasseur, S. Miraux, E. Duguet, C.Sanchez, J. Mater. Chem. 17 (2007) 1563–1569.

[142] J.L.Bridot, A.C.Faure, S.Laurent, C.Rivire, C.Billotey, B.Hiba, M.Janier, V.Josserand, J.L.Coll, L.V.Elst, R. Muller, S.Roux, P.Perriat, O.Tillement, J. Am. Chem. Soc. 129 (2007) 5076–5084.

[143] J.Lee, Y. Lee, J. Youn, H. Na, T. Yu, H.Kim, S. Lee, Y. Koo, J. Kwak, H. Park, H. Chang, M. Hwang, J. Park, J.Kim, T.Hyeon, Small 4 (2008) 143–152.

[144] W. Wu, Q. He, C. Jiang, Nanoscale Res. Lett. 3 (2008) 397–415.

[145] S. Pinho, G. Pereira, P. Voisin, J. Kassem, V. Bouchaud, L. Etienne, J. Peters, L.Carlos, S. Mornet, C. Geraldes, J. Rocha, M. Delville, ACS Nano 4 (2010) 5339–5349.

[146] H. Song, D. Anjum, R. Sougrat, M. Hedhili, N. Khashab, J. of Mat. Chem. 22 (2012) 25003–25010.

[147] H. Zeng, J. Li, J. Liu, Z. Wang, S. Sun, Nature 420 (2002) 395–398.

[148] V. Skumryev, S. Stoyanov, Y. Zhang, G. Hadjipanayis, D. Givord, J. Nogues, Nature 423 (2003) 850–853.

[149] J. Noguès, J. Sort, V. Langlais, V. Skumryev, S. Surinach, J. Munoz, M. Baro, Physics Reports 422 (2005) 65–118.

[150] J. E. Lima, E. L. Winkler, D. Tobia, H. E. Troiani, R. D. Zysler, E. Agostinelli, D. Fiorani, Chem. Mater. 24 (2012) 512–516.

[151] X. Sun, N. F. Huls, A. Sigdel, S. Sun, Nano Lett. 12 (2012) 246–251.

[152] O. Masala, D. Hoffman, N. Sundaram, K. Page, T. Proffen, G. Lawes, R. Seshadri, Solid State Sciences 8 (2006) 1015–1022.

[153] O. Masala, R. Seshadri, J. of the Am. Chem. Soc. 127 (2005) 9354–9355.

[154] B. P. Pichon, O. Gerber, C. Lefevre, I. Florea, S. Fleutot, W. Baaziz, M. Pauly, M. Ohlmann, C. Ulhaq, O. Ersen, V. Pierron-Bohnes, P. Panissod, M. Drillon, S. Begin-Colin, Chem. Mater. 23 (2011) 2886–2900.

[155] F. Aliev, M. Correa-Duarte, A. Mamedov, J.W.Ostrander, M. Giersig, L. Liz-Marzan, N. Kotov, Adv. Mater. 11 (1999) 1006–1011.

[156] H. Zeng, J. Li, Z. Wang, J. Liu, S. Sun, Nano Lett. 4 (2004) 187–190.

[157] M. Mandal, S. Kundu, S. Ghosh, S. Panigrahi, T. Sau, S. Yusuf, T. Pal, Journal of colloid and interface science 286 (2005) 187–194.

[158] J. Lyon, D. Fleming, M. Stone, P. Schiffer, M. Williams, Nanoletters 4 (2004) 719–723.

[159] S. Gaur, S. Johansson, F. Mohammad, C. Kumar, J.J.Spivey, J. of Phys. Chem. C 116 (2012) 22319–22326.

[160] C.Wang, J.Irudayaraj, Small 6 (2010) 283–289.

[161] L.-L. Wang, D. D. Johnson, J. Am. Chem. Soc. 131 (2009) 14023–14029.

[162] E. E. G. Rusakov, L. Son, N. Dubinin, Thermochimica Acta 532 (2012) 103– 106.

[163] A. V. Ruban, H. L. Skriver, J. K. Norskov, Phys. Rev. B 59 (1999) 15990–16000.

[164] A. Tao, S. Habas, P. Yang, small 4 (2008) 310–325.

[165] B. Busbee, S. Obare, C. Murphy, Adv. Mat. 15 (2003) 414–416.

[166] E. Ringe, R. P. V. Duyne, L. D. Marks, Nano Lett. 11 (2011) 3399–3403.

[167] A. S. Barnard, X. M. Lin, L. A. Curtiss, J. Phys. Chem. B 109 (2005) 24465–24472.

[168] H. Ramanarayan, T. Abinandanan, Physica A 318 (2003) 213 – 219.

[169] M. Hillert, J. Rundgren, Phys. Rev. B 32 (1985) 640–642.

[170] M. P. G. Barcaro, A.Fortunelli, L. Rubinovich, Nano Lett. 11 (2011) 1766–1769.

[171] R. V. Chepulskii, W. B. A. van de Walle, S. Curtarolo, Scripta Materialia 62 (2010) 179–182.

[172] G. Wang, M. V. Hove, P. Ross, M. Baskes, Progress in Surface Science 79 (2005) 28–45.

[173] R. T. M. Tsuji, S. Hikino, Y. Sano, Chemistry Letters 38 (2009) 860–861.

[174] M. Tsuji, D. Yamaguchi, M. Matsunaga, M. J. Alam, Crystal Growth & Design 10 (2010) 5129–5135.

[175] I.V.Markov, Crystal Growth for Beginners: Fundamentals of Nucleation, Crystal Growth, and Epitaxy, Singapore: World Scientific, 1995.

[176] F.-R. Fan, D.-Y. Liu, Y.-F. Wu, S. Duan, Z.-X. Xie, Z.-Y. Jiang, , Z.-Q. Tian, J. Am. Chem. Soc. 130 (2008) 6949–6951.

[177] M. Jin, H. Zhang, J. Wang, X. Zhong, N. Lu, Z. Li, Z. Xie, M. J. Kim, Y. Xia, ACS Nano 6 (2012) 2566–2573.

[178] L.Wang, P.Liu, P.Guan, M.Yang, J.Sun, Y.Cheng, A.Hirata, Z.Zhang, E.Ma, X.Han, Nature comm. 4 (2013) 2413 1–6.

[179] M.Chen, E.Ma, K.J.hemker, H.Sheng, Y.Wang, X.Cheng, Science 300 (2003) 1275–1277.

[180] S. V. Gaponenko, Introduction to Nanophotonics, 6 ed., Cambridge University Press, Cambridge, New York, Melbourne, Madrid, Cape Town, Singapore, Sao Paulo, Delhi, Dubai, Tokyo, 2012.

[181] C. Loo, A. Lin, L. Hirsch, M.-H. Lee, J. Barton, N. Halas, J. West, R. Drezek, Technol. Cancer Res. Treat. 3 (2004) 33–40.

[182] M. Brown, T. Suteewong, R. Kumar, V. D'Innocenzo, A. Petrozza, M. M. Lee, U. Wiesner, H. J. Snaith, Nano Lett. 11 (2011) 438–445.

[183] J.Zhang, Y. Tang, K. Lee, M. Ouyang, Science 327 (2010) 1634–1638.

[184] J. Zhang, Y. Tang, K. Lee, M. Ouyang, Nature 466 (2010) 91–95.

[185] K.Aslan, M.Wu, J. Lakowicz, C. Geddes, J. Am. Chem. Soc. 119 (2007) 1524–1525.

[186] M. Viger, L. Live, O. Therrien, D. Boudreau, Plasmonics 3 (2008) 33–40.

[187] O. Tovmachenko, D. van den Heuvel, A. van Blaaderen, H. Gerritsen, Adv. Mater. 18 (2006) 91–95.

[188] D. Cheng, Q. Xu, Chem. Commun. (2007) 248–250.

[189] P.Reineck, D. a nd S.H.Ng, M.Karg, T.Bell, P.Mulvaney, U.Bach, ACS Nano 7 (2013) 6636–6648.

[190] M. Lessard-Viger, M. Rioux, L. Rainville, D. Boudreau, Nano Lett. 9 (2009) 3066–3071.

[191] N. Sui, V. Monnier, Y. Zakharko, Y. Chevolot, S. Alekseev, J.-M. Bluet, V. Lysenko, E. Souteyrand, Plasmonics 3 (2012) 1–8.

[192] J.-F. Li, Y. F. Huang, Y. Ding, Z.-L. Yang, S. B. Li, X. S. Zhou, F. R. Fan, W. Zhang, Z. Y. Zhou, D. Y. Wu, B. Ren, Z.-L. Wang, Z.-Q. Tian, Nature 464 (2010) 392–395.

[193] N. M. Lawandy, Appl Phys Lett 85 (2004) 5040–5042.

[194] S.-Y. Liu, J. Li, F. Zhou, L. Gan, Z.-Y. Li, Opt. Lett. 36 (2011) 1296–1298.

[195] M. A. Noginov, G. Zhu, A. M. Belgrave, R. Bakker, V. M. Shalaev, E. E. Narimanov, S. Stout, E. Herz, T. Suteewong, U. Wiesner, Nature 460 (2009) 1110–1112.

[196] D. Bergman, M. I. Stockman, Phys. Rev. Lett. 90 (2003) 027402 1–4.

[197] D. Bergman, M. I. Stockman, Laser Phys. 14 (2004) 409–411.

[198] M. I. Stockman, Nature Photon. 2 (2008) 327–329.

[199] M. I. Stockman, J Opt-UK 12 (2010) 024004 1–13.

[200] K. Kawaguchi, J. Jaworski, Y. Ishikawa, T. Sasaki, N.Koshizaki, J. of Mag. and Mag. Mat. 310 (2007) 2369–2371.

[201] M. Mikhaylova, D. Kim, N. Bobrysheva, M. Osmolowsky, V. Semenov, T.Tsakalakos, M. Muhammed, Langmuir 20 (2004) 2472–2477.

[202] Z. Xu, Y. Hou, S.Sun, J. of the Am. Chem. Soc. 129 (2007) 8698–8699.

[203] C. Levin, C. Hofmann, T. Ali, A. Kelly, E. Morosan, P. Nordlander, K. Whitmire, N. Halas, ACS nano 3 (2009) 1379–1388.

[204] F.Pineider, C. de Julián Fernández, V. Videtta, E. Carlino, A. al Hourani, F. Wilhelm, A. Rogalev, P. D. Cozzoli, P. Ghigna, C. Sangregorio, ACS nano 7 (2013) 857866.

[205] H. Yin, Z. Ma, M. Chi, S. Dai, Catalysis Today 160 (2011) 87–95.

[206] K. Yu, Z. Wu, Q. Zhao, B. Li, Y. Xie, The J. of Phys. Chem. C 112 (2008) 2244–2247.

[207] T. Ming, L. Zhao, H. Chen, K. C. Woo, J. Wang, H. Lin, Nano Lett. 11 (2011) 2296–2303.

[208] J. Lakowicz, M. Chowdhury, H. Szmacinski, Y. Fu, J. Zhang, K. Nowaczyk, Analyst 133 (2008) 1308–1346.

[209] M. Li, X.-F. Yu, S. Liang, X.-N. Peng, Z.-J. Yang, Y.-L. Wang, Q.-Q. Wang, Adv. Funct. Mater. 21 (2011) 1788–1794.

[210] S. Neretina, E. Dreaden, W. Qian, M. A. El-Sayed, R. A. Hughes, J. S. Preston, P. Mascher, Nano Lett. 9 (2009) 3772–3779.

[211] Y. Pu, R. Grange, C.-L. Hsieh, D. Psaltis, Phys. Rev. Lett. 104 (2010) 207402 1–4.